Selective imaging of extended reflectors in a two-dimensional waveguide

Chrysoula Tsogka and Dimitris Mitsoudis and Symeon Papadimitropoulos

Selective imaging of extended reflectors in a two-dimensional waveguide

Chrysoula Tsogka[1,2], Dimitrios A. Mitsoudis[3,2], Symeon Papadimitropoulos[1]

[1]Department of Applied Mathematics, University of Crete, Heraklion 71409, Greece
[2]Institute of Applied and Computational Mathematics, FORTH, Heraklion 71110, Greece.
[3]Archimedes Center for Modeling, Analysis & Computation (ACMAC), Department of Applied Mathematics, University of Crete, Heraklion 71003, Greece.

E-mail: tsogka@tem.uoc.gr, dmits@tem.uoc.gr, spapadem@tem.uoc.gr

Abstract. We consider the problem of selective imaging extended reflectors in waveguides using the response matrix of the scattered field obtained with an active array. Selective imaging amounts to being able to focus at the edges of a reflector which typically give raise to weaker echoes than those coming from its main body. To this end, we propose a selective imaging method that uses projections on low rank subspaces of a weighted modal projection of the array response matrix, $\widehat{\mathbb{P}}(\omega)$. We analyze theoretically our imaging method for a simplified model problem where the scatterer is a vertical one-dimensional perfect reflector. In this case, we show that the rank of $\widehat{\mathbb{P}}(\omega)$ equals the size of the reflector devided by the cross-range array resolution which is $\lambda/2$ for an array spanning the whole depth of the waveguide. We also derive analytic expressions for the singular vectors of $\widehat{\mathbb{P}}(\omega)$ which allows us to show how selective imaging can be achieved. Our numerical simulations are in very good agreement with the theory and illustrate the robustness of our imaging functional for reflectors of various shapes.

1. Introduction

In this work we consider the problem of detecting and imaging *extended* reflectors submerged in the sea, using acoustic waves produced by an active array. The array consists of N transducers that act as sources and receivers. The data that we are going to use for imaging are assumed to be given in the form of the so called *array response matrix* in the frequency domain, i.e., an $N \times N$ complex matrix whose entries are the Fourier transforms of the time traces of the echoes recorded in all receivers when each source emits a signal. The term 'extended' refers to reflectors which are comparable in size to the acoustic wavelength. Here, the sea is modeled as an acoustic waveguide consisting of a single homogeneous water layer confined above by the sea surface and below by the seafloor, both assumed to be horizontal. Thus, our waveguide is an infinite strip of constant depth.

The imaging problem that we wish to solve is the following: Assuming that the extended reflector is illuminated by an active vertical array which spans the whole depth of the waveguide, and that the array response matrix is known, we want to image an extended reflective scatterer located in the waveguide. To this end we define a search domain (a bounded subset of our waveguide) and use appropriate imaging functionals, which have the property that their values, when they are computed and graphically displayed in the search domain, exhibit peaks that indicate the presence of the scatterer. Examples of such imaging functionals include the *Kirchhoff migration functional* (see [4, 5]) and the *matched field functional* (see [18]).

Another question that often arises in imaging of extended reflectors is whether we can create an image which focuses on specific parts of the scatterer. A way to achieve this is by a *selective imaging* technique called the subspace projection method [7]. This method is based on the singular value decomposition (SVD), see for example [11, §2.5], of the array response matrix, which helps us to create a filtered version of it which, in turn, will be used for imaging purposes. This technique has been employed in [7] to image extended scatterers embedded in a homogeneous medium, while in [8] the authors considered selective imaging in clutter, i.e., propagation media with inhomogeneities that are unknown, cannot be estimated in detail, and, are modeled as random processes.

The concept of selective imaging of extended scatterers has been motivated by the concept of *selective focusing*, which concerns the case where there are multiple point (or small) scatterers in the medium and, essentially, allows one to distinguish specific scatterers by creating images that focus separately in each one of them. In this direction, the work of Prada and Fink [22] has been very influential. They have introduced the so-called DORT method (DORT is an acronym for 'decomposition of the time reversal operator' in French), which uses the singular value decomposition of the time reversal operator to focus selectively on scattering obstacles. The experimental results obtained in [22] show that for small scatterers, the number of nonzero (or significant) singular values of the response matrix is exactly the number of obstacles contained in the medium. Furthermore, the use of the corresponding singular vectors as incident field results

in selective focusing on the scatterers, provided that pairwise they are located at a sufficiently long-distance apart. Related works include [20, 23]. When the scatterers are clustered together, the one-to-one correspondence between the singular vectors of the response matrix and the scatterers does not hold any more, and as a consequence, selective focusing cannot be achieved with DORT. This issue was addressed in [6] where selective focusing was achieved by using as illumination an optimal convex combination of the leading singular vectors across the bandwidth. To the best of our knowledge, the first rigorous mathematical justification of DORT has been given in [16], where the propagation medium is the free space $\mathbb{R}^3$. For the analysis of DORT in a waveguide environment we refer to the work of Pinçon and Ramdani [21].

The main goal of the present work is to propose and analyze a selective imaging method of extended reflectors in waveguides. Moreover, we want to investigate whether, and how, the number of 'significant' (non-zero) singular values of the array response matrix is related to the size of the reflector. Relevant works in the same spirit, but for the free space case, include [27], where an analysis of the response matrix for extended reflectors is presented, and [7], where the subspace projection method has been analyzed and a relation between the number of significant singular values and the size of the reflector has been derived.

This work is organized as follows. In Section 2, we formulate the problem, present the basic features of wave propagation in waveguides and introduce the relevant notation and terminology. In Section 3 we present the imaging functionals that will be used throughout this work. These are the Kirchhoff migration functional and an alternative imaging functional, based on a weighted projection of the response matrix on the propagating modes. In Section 4, we present the outcome of some numerical experiments for a circle, a rhombus and a square shaped scatterer. Section 5 is devoted to the theoretical analysis of the imaging method for a simplified model problem where the scatterer is a crack, i.e., a vertical one-dimensional perfect reflector. For this model problem, we derive a relation between the number of significant singular values of the array response matrix and the size of our scatterer. Specifically, we show that the number of significant singular values equals the size of the scatterer divided by the array resolution. This result which is intuitive was derived in [7] for the free space and is, to the best of our knowledge, a new one concerning the waveguide geometry. We also explore the form of the singular vectors of the response matrix in order to gain some insight regarding selective imaging features. We end with some concluding remarks in Section 6, while in the Appendix a resolution analysis for the proposed imaging functional is performed.

2. Formulation of the problem

We consider the problem of detecting and imaging extended scatterers submerged in the sea using acoustic waves. More precisely, we model a marine environment by an infinite two-dimensional waveguide $\mathbb{R} \times (0, D)$ in Cartesian coordinates (z, x), where z

denotes the range variable, and x the depth (cross-range) variable taken to be positive downward. Troughout this paper, vectors in $\mathbb{R}^n$ are denoted by boldface characters while vectors in $\mathbb{R}\times(0,D)$ are denoted by boldface characters with an overscript arrow. Our waveguide consists of a single water layer, with constant density and constant sound speed c_0. A single extended scatterer denoted by $\mathcal{O}$ is submerged in the water layer, see Figure 1. The term 'extended' indicates that the typical size of the scatterer is comparable to the wavelength.

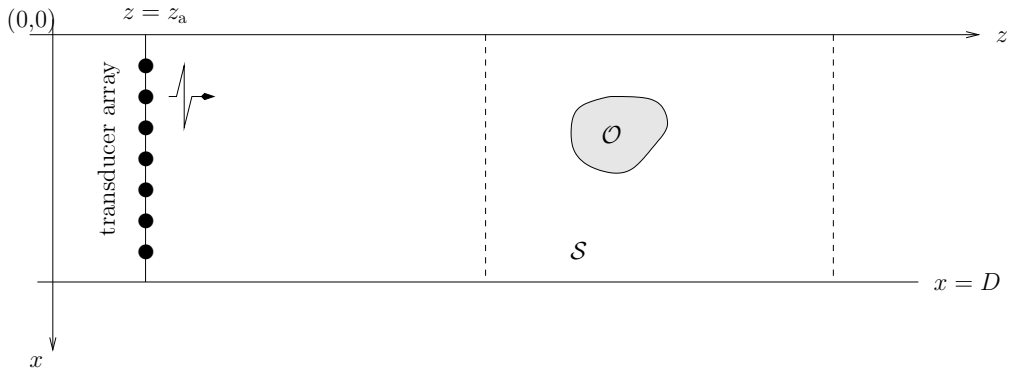

Figure 1: Schematic representation of our waveguide problem and of the active array imaging setup.

We assume that the total acoustic pressure field $p^{\rm tot}(t,\vec{\boldsymbol{x}})$ satisfies the wave equation

$$\Delta p^{\rm tot}(t,\vec{\boldsymbol{x}}) - \frac{1}{c_0^2}\frac{\partial^2 p^{\rm tot}(t,\vec{\boldsymbol{x}})}{\partial t^2} = f(t,\vec{\boldsymbol{x}}), \tag{1}$$

where the source term is of the form $f(t,\vec{\boldsymbol{x}}) = -\exp(\mathrm{i}\omega t)\delta(\vec{\boldsymbol{x}}-\vec{\boldsymbol{x}}_{\rm s})$, modelling a point-like source with time harmonic dependence located at $\vec{\boldsymbol{x}}_{\rm s}$. The scatterer is assumed to be sound-hard, hence a homogeneous Neumann condition is posed on its boundary $\partial\mathcal{O}$. Equation (1) is supplemented with pressure release boundary conditions on the surface and the seafloor, and we also assume that $p^{\rm tot}(t,\vec{\boldsymbol{x}}) = 0$ for $t \le 0$, expressing that the medium is quiescent before emission. Taking the Fourier transform

$$\widehat{p}^{\rm tot}(\omega,\vec{\boldsymbol{x}}) = \int \mathrm{e}^{\mathrm{i}\omega t} p^{\rm tot}(t,\vec{\boldsymbol{x}})\,dt,$$

we obtain from (1) the Helmholtz equation

$$-\Delta\widehat{p}^{\rm tot}(\omega,\vec{\boldsymbol{x}}) - k^2\widehat{p}^{\rm tot}(\omega,\vec{\boldsymbol{x}}) = \delta(\vec{\boldsymbol{x}}-\vec{\boldsymbol{x}}_{\rm s}), \tag{2}$$

where $k = \omega/c_0$ is the real wavenumber, $\omega = 2\pi/\lambda$ is the angular frequency, and λ is the wavelength.

Now, let $\{\mu_n, X_n\}_{n=1,2,\ldots}$ denote the eigenvalues and corresponding orthonormal eigenfunctions of the two-point vertical eigenvalue problem

$$X''(x) + \mu X(x) = 0,\ x\in(0,D) \quad \text{and} \quad X(0) = X(D) = 0,$$

i.e.,

$$\mu_n = (n\pi/D)^2, \quad X_n(x) = \sqrt{2/D}\sin(\sqrt{\mu_n}x),\ n = 1,2,\ldots. \tag{3}$$

The family of eigenfunctions $\{X_n\}_{n=1,2,\dots}$ forms an orthonormal basis of $L^2[0,D]$. We assume that for each frequency there exists an index M such that

$$\mu_M < k < \mu_{M+1},$$

or, in other words, that the wavenumber does not coincide with any of the mode cutoff frequencies, and the first M eigenvalues correspond to the *propagating* modes, while the rest to the *evanescent* modes. Let us also denote the horizontal wavenumbers by

$$\beta_n = \begin{cases} \sqrt{k^2-\mu_n}, & 1 \le n \le M, \\ \mathrm{i}\sqrt{\mu_n - k^2}, & n \ge M+1. \end{cases} \tag{4}$$

Moreover, let $\widehat{G}(\vec{\boldsymbol{x}}, \vec{\boldsymbol{x}}_{\mathrm{s}})$ be the outgoing Green's function of the Helmholtz operator $-\Delta \cdot -k^2\cdot$, evaluated at $\vec{\boldsymbol{x}} = (z,x) \in \mathbb{R}\times(0,D)$ due to a point source located at $\vec{\boldsymbol{x}}_{\mathrm{s}} = (z_{\mathrm{s}}, x_{\mathrm{s}})$. (In the underwater acoustics community a point source in plane geometry is usually referred to as a line source, [17].) Then it is well known, see, e.g., [17, 21], that $\widehat{G}$ admits the following normal mode representation

$$\widehat{G}(\vec{\boldsymbol{x}}, \vec{\boldsymbol{x}}_{\mathrm{s}}) = \frac{\mathrm{i}}{2}\sum_{n=1}^{\infty} \frac{1}{\beta_n} \mathrm{e}^{\mathrm{i}\beta_n |z-z_{\mathrm{s}}|} X_n(x) X_n(x_{\mathrm{s}}), \tag{5}$$

where $\{\mu_n, X_n\}$ and β_n are defined in (3) and (4), respectively.

2.1. Array imaging setup

We consider a one-dimensional vertical active array spanning the whole depth of the waveguide and located at range $z = z_{\mathrm{a}} \ge 0$, see Figure 1. The array consists of N transducers which act both as sources and receivers, and, we assume that they are closely spaced and uniformly distributed on the array with an inter-element array distance $h = D/(N+1)$; h is usually called the array *pitch*.

Let, also, $\widehat{\Pi}(\omega)$ denote the $N\times N$ complex *array response matrix* in the frequency domain, whose (r,s) entry is defined as the Fourier transform of the time traces recorded at the r-th transducer due to a δ–function impulse generated by the s-th transducer, for a given frequency ω. In what follows, the data that we are going to use for imaging is the array response matrix for the scattered field in the frequency domain, created by subtracting the array response matrix for the incident field from the corresponding one for the total field.

3. Imaging

Let us first define the search domain $\mathcal{S}$, as a bounded subdomain of our waveguide that may contain a scatterer. $\mathcal{S}$ is discretized, using a rectangular grid, and $\vec{\boldsymbol{y}}^{\mathrm{s}} = (z^{\mathrm{s}}, x^{\mathrm{s}})$ denotes an arbitrary node in $\mathcal{S}$. We are interested in creating an image of the search domain $\mathcal{S}$. A classical imaging method is *Kirchhoff migration (KM)*, [4, 5], defined by,

$$\mathcal{I}^{\mathrm{KM}}(\vec{\boldsymbol{y}}^{\mathrm{s}}, \omega) = \sum_{r=1}^{N} \overline{\widehat{G}(\vec{\boldsymbol{x}}_r, \vec{\boldsymbol{y}}^{\mathrm{s}}, \omega)} \sum_{s=1}^{N} \widehat{\Pi}(\vec{\boldsymbol{x}}_r, \vec{\boldsymbol{x}}_s, \omega)\, \overline{\widehat{G}(\vec{\boldsymbol{x}}_s, \vec{\boldsymbol{y}}^{\mathrm{s}}, \omega)}, \tag{6}$$

for a single frequency ω and $\vec{\boldsymbol{y}}^{\mathrm{s}} \in \mathcal{S}$. Here the bars denote complex conjugation. KM consists in backpropagating the signals from each receiver $\vec{\boldsymbol{x}}_r$ to a point $\vec{\boldsymbol{y}}^{\mathrm{s}}$ in the search domain and then back to the source $\vec{\boldsymbol{x}}_s$. The image is the sum of the backpropagated signals for all sources and receivers.

In (6) we have defined the imaging functional for a single frequency ω. When we have multi-frequency data, we can compute instead,

$$\mathcal{I}^{\mathrm{KM}}(\vec{\boldsymbol{y}}^{\mathrm{s}}) = \Big|\sum_{\omega} \mathcal{I}^{\mathrm{KM}}(\vec{\boldsymbol{y}}^{\mathrm{s}}, \omega)\Big|. \tag{7}$$

KM is widely used in seismic imaging and exploration geophysics; typically in these applications the arrays and the bandwidth are very large. This is a setup in which perfect imaging resolution can be achieved. Indeed, in that case the ideal point spread function (i.e., the image of a point scatterer), which is a Dirac distribution, can be obtained at least asymptotically as the array aperture and the bandwidth tend to infinity (cf. [4]). To be more precise this result is obtained for a slight modification of (6) that uses a weighing factor which takes into account the source–receiver geometry.

3.1. Selective imaging

In selective imaging we are interested in reconstructing specific parts of the reflector like, for example, its boundary. A way to achieve this is by means of the subspace projection method [7], which is based on the singular value decomposition (SVD) of the $N \times N$ array response matrix $\widehat{\Pi}(\omega)$ in the frequency domain. As remarked in [7], the SVD of $\widehat{\Pi}(\omega)$ may serve as a filter which enables us to identify reflections emanating from the edges of the scatterer. Such reflections are typically weaker than, and therefore masked by, those coming from the body of the scatterer. The SVD of $\widehat{\Pi}(\omega)$ is a factorization of the form (see, for example, [11, §2.5])

$$\widehat{\Pi}(\omega) = U(\omega)\Sigma(\omega)V^*(\omega),$$

where Σ is a diagonal matrix containing the singular values σ_i of $\widehat{\Pi}(\omega)$ in descending order, and U, V are unitary matrices containing the left and right singular vectors, respectively. For the rest of this section, we will occasionally omit the ω's for sake of notational convenience.

Now, let us write the SVD of $\widehat{\Pi}(\omega)$ as a sum of the form:

$$\widehat{\Pi}(\omega) = \sum_{i=1}^{\rho} \sigma_i U_i V_i^*,$$

where $\rho = \mathrm{rank}(\widehat{\Pi}(\omega))$, so that $\sigma_1 \geq \ldots \geq \sigma_\rho > \sigma_{\rho+1} = \ldots = \sigma_N = 0$, and U_i, V_i are the left and right singular vectors, respectively. Then a filtered version of the response matrix may be written in the form:

$$D[\widehat{\Pi}(\omega)] = \sum_{i=1}^{\rho} d_i \sigma_i U_i V_i^*,$$

where the coefficients d_i are called the filter weights. We will simply consider $d_i \in \{0, 1\}$, which amounts to saying that if $d_i = 1$ then the i-th singular vector is taken into account in the filtered version of the response matrix, while if $d_i = 0$ it is not.

We will assume hereinafter, that the scatterer and the search domain are located far enough from the array to allow us to retain only the propagating modes in (5). Then, replacing $\widehat{G}$, given by (5), into (6) we may write the KM functional in the form

$$\mathcal{I}^{\mathrm{KM}}(\vec{\boldsymbol{y}}^{\mathrm{s}}, \omega) = -\frac{1}{4} \sum_{s,r=1}^{N} \widehat{\Pi}(\vec{\boldsymbol{x}}_r, \vec{\boldsymbol{x}}_s, \omega) \times \\ \times \sum_{m,n=1}^{M} \frac{\mathrm{e}^{-\mathrm{i}(\beta_m+\beta_n)|z_{\mathrm{a}}-z^{\mathrm{s}}|}}{\beta_m \beta_n} X_m(x_s) X_m(x^{\mathrm{s}}) X_n(x_r) X_n(x^{\mathrm{s}}). \tag{8}$$

Let us also define the functional

$$\mathcal{I}^{\mathrm{KM,f}}(\vec{\boldsymbol{y}}^{\mathrm{s}}, \omega) = -\frac{1}{4} \sum_{s,r=1}^{N} \Big(D[\widehat{\Pi}(\omega)] \Big)_{rs} \times \\ \times \sum_{m,n=1}^{M} \frac{\mathrm{e}^{-\mathrm{i}(\beta_m+\beta_n)|z_{\mathrm{a}}-z^{\mathrm{s}}|}}{\beta_m \beta_n} X_m(x_s) X_m(x^{\mathrm{s}}) X_n(x_r) X_n(x^{\mathrm{s}}), \tag{9}$$

derived by replacing the full response matrix by its filtered version. For multi-frequency data, we define

$$\mathcal{I}^{\mathrm{KM,f}}(\vec{\boldsymbol{y}}^{\mathrm{s}}) = \Big| \sum_{\omega} \mathcal{I}^{\mathrm{KM,f}}(\vec{\boldsymbol{y}}^{\mathrm{s}}, \omega) \Big|. \tag{10}$$

Finally, we introduce the functionals

$$\mathcal{I}_J^{\mathrm{KM}}(\vec{\boldsymbol{y}}^{\mathrm{s}}, \omega) = -\frac{1}{4} \sum_{s,r=1}^{N} \left(\sigma_J(\omega) U_J(\omega) V_J^*(\omega) \right)_{rs} \times \\ \times \sum_{m,n=1}^{M} \frac{\mathrm{e}^{-\mathrm{i}(\beta_m+\beta_n)|z_{\mathrm{a}}-z^{\mathrm{s}}|}}{\beta_m \beta_n} X_m(x_s) X_m(x^{\mathrm{s}}) X_n(x_r) X_n(x^{\mathrm{s}}), \tag{11}$$

and

$$\mathcal{I}_J^{\mathrm{KM}}(\vec{\boldsymbol{y}}^{\mathrm{s}}) = \Big| \sum_{\omega} \mathcal{I}_J^{\mathrm{KM}}(\vec{\boldsymbol{y}}^{\mathrm{s}}, \omega) \Big|, \tag{12}$$

which are derived from (9) and (10), respectively, when $d_J = 1$ and $d_i = 0$ for all $i \neq J$; in other words, when we consider projection on the single J-th singular vector of the response matrix.

3.2. Modal projection and selective imaging

For an array spanning the whole waveguide depth with an array pitch h small enough, we can approximate the double sum in (8) by a double integral over $[0, D]$, to get,

$$\mathcal{I}^{\mathrm{KM}}(\vec{\boldsymbol{y}}^{\mathrm{s}}, \omega) \approx -\frac{1}{4h^2} \int_0^D \mathrm{d}x_s \int_0^D \mathrm{d}x_r \, \widehat{\Pi}(\vec{\boldsymbol{x}}_s, \vec{\boldsymbol{x}}_r, \omega) \times$$

$$\times \sum_{m,n=1}^{M} \frac{\mathrm{e}^{-\mathrm{i}(\beta_m+\beta_n)|z_\mathrm{a}-z^\mathrm{s}|}}{\beta_m\beta_n} X_m(x_s)X_m(x^\mathrm{s})X_n(x_r)X_n(x^\mathrm{s})$$

$$= -\frac{1}{4h^2}\sum_{m,n=1}^{M} \frac{\mathrm{e}^{-\mathrm{i}(\beta_m+\beta_n)|z_\mathrm{a}-z^\mathrm{s}|}}{\beta_m\beta_n} X_m(x^\mathrm{s})X_n(x^\mathrm{s}) \times$$

$$\times \int_0^D \int_0^D \widehat{\Pi}(\vec{\boldsymbol{x}}_s, \vec{\boldsymbol{x}}_r, \omega) X_m(x_s)X_n(x_r)\, \mathrm{d}x_r\, \mathrm{d}x_s. \tag{13}$$

Now, let us introduce an $M \times M$ matrix $\widehat{\mathbb{Q}}(\omega)$, with entries

$$\widehat{\mathbb{Q}}_{mn}(\omega) = \int_0^D \mathrm{d}x_s \int_0^D \mathrm{d}x_r\, \widehat{\Pi}(\vec{\boldsymbol{x}}_s, \vec{\boldsymbol{x}}_r, \omega) X_m(x_s)X_n(x_r), \tag{14}$$

for $m, n = 1, 2, \ldots, M$.

In view of (14), (13) may be equivalently written as

$$\mathcal{I}^{\mathrm{KM}}(\vec{\boldsymbol{y}}^\mathrm{s}, \omega) \approx -\frac{1}{4h^2}\sum_{m,n} \frac{\mathrm{e}^{-\mathrm{i}(\beta_m+\beta_n)|z_\mathrm{a}-z^\mathrm{s}|}}{\beta_m\beta_n} X_n(x^\mathrm{s})X_m(x^\mathrm{s})\widehat{\mathbb{Q}}_{mn}(\omega). \tag{15}$$

Instead of using (15) we propose to use the following imaging functional

$$\widetilde{\mathcal{I}}^{\mathrm{KM}}(\vec{\boldsymbol{y}}^\mathrm{s}, \omega) = -\frac{1}{4h^2}\sum_{m,n=1}^{M} \mathrm{e}^{-\mathrm{i}(\beta_m+\beta_n)|z_\mathrm{a}-z^\mathrm{s}|} X_n(x^\mathrm{s})X_m(x^\mathrm{s})\widehat{\mathbb{P}}_{mn}(\omega), \tag{16}$$

where the $M \times M$ matrix $\widehat{\mathbb{P}}$ is defined as

$$\widehat{\mathbb{P}}_{mn}(\omega) = \beta_m\beta_n\widehat{\mathbb{Q}}_{mn}, \quad m, n = 1, \ldots, M. \tag{17}$$

Note that $\widehat{\mathbb{P}}_{mn}(\omega)$ is a weighted modal projection of the array response matrix. Our numerical results indicate (see Section 4) that (16) is a robust selective imaging functional while this is not the case for (15). Our choice of imaging with (16) is also justified by the theoretical analysis carried out in Section 5 for the case of a simple scatterer geometry.

For multi-frequency data, we define

$$\widetilde{\mathcal{I}}^{\mathrm{KM}}(\vec{\boldsymbol{y}}^\mathrm{s}) = \Big|\sum_{\omega} \widetilde{\mathcal{I}}^{\mathrm{KM}}(\vec{\boldsymbol{y}}^\mathrm{s}, \omega)\Big|. \tag{18}$$

We also introduce functionals for selective imaging, as we have done in (9)–(12), using filtered versions of $\widehat{\mathbb{P}}$. The only thing that changes in this process is the size of the response matrix. Now, we are dealing with an $M \times M$ matrix, where M denotes the number of propagating modes. Specifically, for a single frequency ω, let

$$\widetilde{\mathcal{I}}^{\mathrm{KM,f}}(\vec{\boldsymbol{y}}^\mathrm{s}, \omega) = -\frac{1}{4h^2}\sum_{m,n=1}^{M} \mathrm{e}^{-\mathrm{i}(\beta_n+\beta_m)|z_\mathrm{a}-z^\mathrm{s}|} X_n(x^\mathrm{s})X_m(x^\mathrm{s}) \left(D[\widehat{\mathbb{P}}(\omega)]\right)_{mn}, \tag{19}$$

while for multi-frequency data we define

$$\widetilde{\mathcal{I}}^{\mathrm{KM,f}}(\vec{\boldsymbol{y}}^\mathrm{s}) = \Big|\sum_{\omega} \widetilde{\mathcal{I}}^{\mathrm{KM,f}}(\vec{\boldsymbol{y}}^\mathrm{s}, \omega)\Big|. \tag{20}$$

Furthermore, we define

$$\widetilde{\mathcal{I}}_J^{\mathrm{KM}}(\vec{\boldsymbol{y}}^{\mathrm{s}},\omega) = -\frac{1}{4h^2}\sum_{m,n=1}^{M} \mathrm{e}^{-\mathrm{i}(\beta_n+\beta_m)|z_{\mathrm{a}}-z^{\mathrm{s}}|} \times \\ \times X_n(x^{\mathrm{s}})X_m(x^{\mathrm{s}})\Big(\sigma_J(\omega)U_J(\omega)V_J^*(\omega)\Big)_{mn}, \tag{21}$$

and

$$\widetilde{\mathcal{I}}_J^{\mathrm{KM}}(\vec{\boldsymbol{y}}^{\mathrm{s}}) = \Big|\sum_{\omega}\widetilde{\mathcal{I}}_J^{\mathrm{KM}}(\vec{\boldsymbol{y}}^{\mathrm{s}},\omega)\Big|, \tag{22}$$

where by abusing slightly the notation we denote by $\sigma_J(\omega)U_J(\omega)V_J^*(\omega)$ the projection on the J-th singular vector of $\widehat{\mathbb{P}}(\omega)$.

4. Numerical experiments

In this section we present the outcome of some numerical experiments that we have performed with scatterers of various shapes and sizes. In order to construct the array response matrix, which is necessary for evaluating the imaging functionals, we solve numerically the wave equation problem (1). To this end, we use Montjoie [19], a high-order finite element C++ code developed in INRIA, designed to solve problems arising in wave propagation phenomena, such as acoustic, electromagnetic, aeroacoustic and elastodynamic problems.

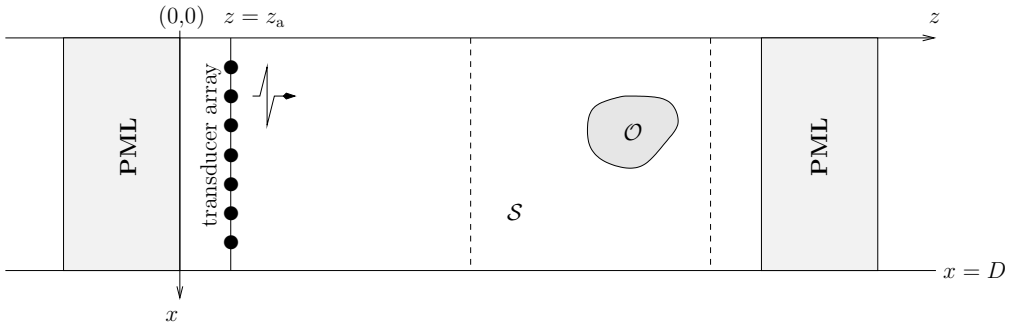

Figure 2: Schematic representation of a waveguide truncated near and far from the source with two perfectly matched layers.

We consider a waveguide with depth equal to $D = 200$ m and sound speed $c_0 = 1500$ m/s. The vertical array is placed at $z_{\mathrm{a}} = 40$ m and consists of $N = 39$ transducers uniformly distributed in the water column with a pitch $h = 5$ m. Point-like sources are simulated by considering the source term in (1) to be of the form $f(t,\vec{\boldsymbol{x}}) = h(t)\, g(\vec{\boldsymbol{x}};\vec{\boldsymbol{x}}_s)$. Here $h(t)$ is a Ricker function of time, given by

$$h(t) = \sqrt{2}f_0\left[1-4\pi^2 f_0^2(t-t_c))^2\right]\exp\left\{-[\sqrt{2}\pi f_0(t-t_c)]^2\right\},$$

where f_0 is the central frequency of the pulse and t_c is the time at which the source attains its maximum. In all experiments that we will show here $f_0 = 75$ Hz, $t_c = 0.01$ s

and the final computation time is taken equal to $T = 4$ s. The function $g(\vec{\boldsymbol{x}}; \vec{\boldsymbol{x}}_s)$ is a Gaussian, given by $g(\vec{\boldsymbol{x}}; \vec{\boldsymbol{x}}_s) = \sqrt{2\pi/\alpha}\exp(-\alpha|\vec{\boldsymbol{x}} - \vec{\boldsymbol{x}}_s|^2)$, where $\alpha = \ln(10^6)/r^2$; r determines the support of the Gaussian and is taken equal to 10 m.

The originally infinite (in the z-direction) domain is truncated by introducing two perfectly matched layers (PML) [3, 9], see Figure 2. The one near the source is confined in range in $[-100, 0]$, while the other, far from the source, in $[500, 600]$ (all distances are in meters). We have checked that the width of 100 m for the PML was enough in order to absorb the waves efficiently. The resulting computational domain is discretized with quadrangles (mainly squares, unless otherwise indicated) on which the usual basis functions of the $\mathbb{Q}_n$ family ($\mathbb{Q}_n = \text{span}\{x^\ell y^m,\ 0 \le \ell, m \le n\}$) for $n = 4$ are used. Numerical quadrature is based on Gauss-Lobatto rules, and time discretization employs a fourth–order Leapfrog scheme.

In all cases the frequencies that are used are close to a central reference frequency $f_0 = 75$ Hz, for which the corresponding wavelength is equal to $\lambda_0 = 20$ m. In particular, we consider frequencies ranging from 70.5 to 79.5 Hz with an increment of 1 Hz, unless otherwise stated.

In what follows we will examine the performance of the imaging functionals $\mathcal{I}^{\text{KM}}$ and $\widetilde{\mathcal{I}}^{\text{KM}}$. Let us recall the results for selective imaging in free space: it was shown in [7] that information about the edges of a reflector is contained in those singular vectors that correspond to singular values of the response matrix that lie in the intermediate regime between the large ones and zero. In our numerical simulations we observe the same behaviour for imaging in waveguides with $\widetilde{\mathcal{I}}^{\text{KM}}$ while this is not the case for $\mathcal{I}^{\text{KM}}$. The behaviour of $\widetilde{\mathcal{I}}^{\text{KM}}$ will be explained with the analysis carried out in Section 5.

Test case 1: Circular scatterer with diameter $\delta = 40$ m. We consider here a circular scatterer with diameter $\delta = 2\lambda_0 = 40$ m centered at (440,100) m. Figure 3 depicts the singular values (normalized with respect to the largest one) of the matrices $\widehat{\Pi}$ and $\widehat{\mathbb{P}}$ for a frequency equal to 75.5 Hz. As expected, only few of the singular values are nonzero.

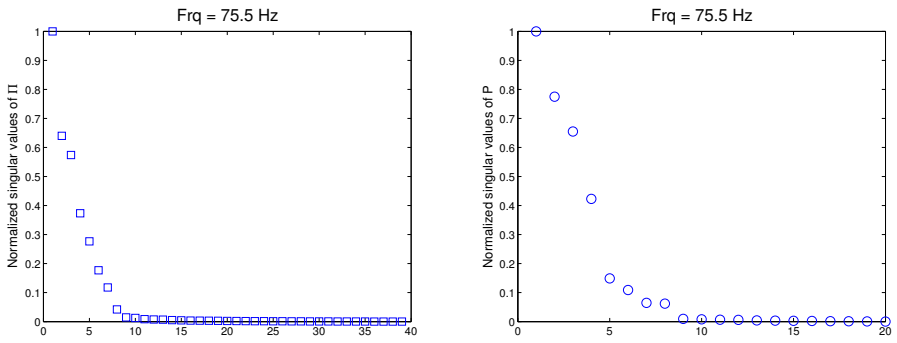

Figure 3: Normalized singular values of $\widehat{\Pi}$ (left subplot) and $\widehat{\mathbb{P}}$ (right subplot) for a circle scatterer with diameter $b = 40$ m.

In Figure 4 we plot the values of $\mathcal{I}^{\text{KM}}$ and $\widetilde{\mathcal{I}}^{\text{KM}}$ when the full matrices $\widehat{\Pi}$ and $\widehat{\mathbb{P}}$, respectively, are used. In both cases we see that the front part of the circle is recovered,

although for $\widetilde{\mathcal{I}}^{\mathrm{KM}}$ the image is supported mainly around the center of the circle at $x = 100$ m.

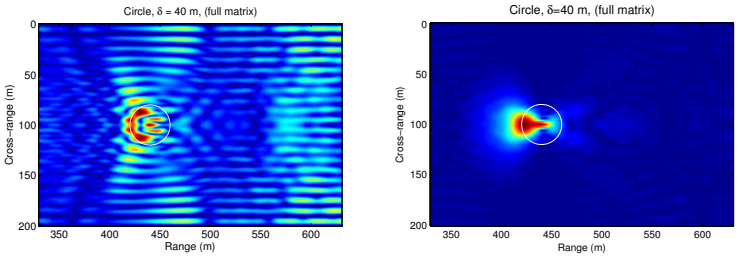

Figure 4: $\mathcal{I}^{\mathrm{KM}}$ (left subplot) versus $\widetilde{\mathcal{I}}^{\mathrm{KM}}$ (right subplot) for a circular scatterer with diameter $\delta = 40$ m.

In Figure 5 we present the results of selective imaging with $\mathcal{I}_J^{\mathrm{KM}}$ and $\widetilde{\mathcal{I}}_J^{\mathrm{KM}}$ (see (12) and (22), respectively), for $J = 1$, 4 and 5. For $J = 1$, $\mathcal{I}_J^{\mathrm{KM}}$ focuses towards the endpoints of the vertical diameter of the circle, while $\widetilde{\mathcal{I}}_J^{\mathrm{KM}}$ in the front center of the circle. For $J = 4$, $\mathcal{I}_J^{\mathrm{KM}}$ seems to focus in the two endpoints of the horizontal diameter of the circle and $\widetilde{\mathcal{I}}_J^{\mathrm{KM}}$ towards the endpoints of the vertical diameter. For $J = 5$, both $\mathcal{I}_J^{\mathrm{KM}}$ and $\widetilde{\mathcal{I}}_J^{\mathrm{KM}}$ seem to locate roughly the boundary of the circle.

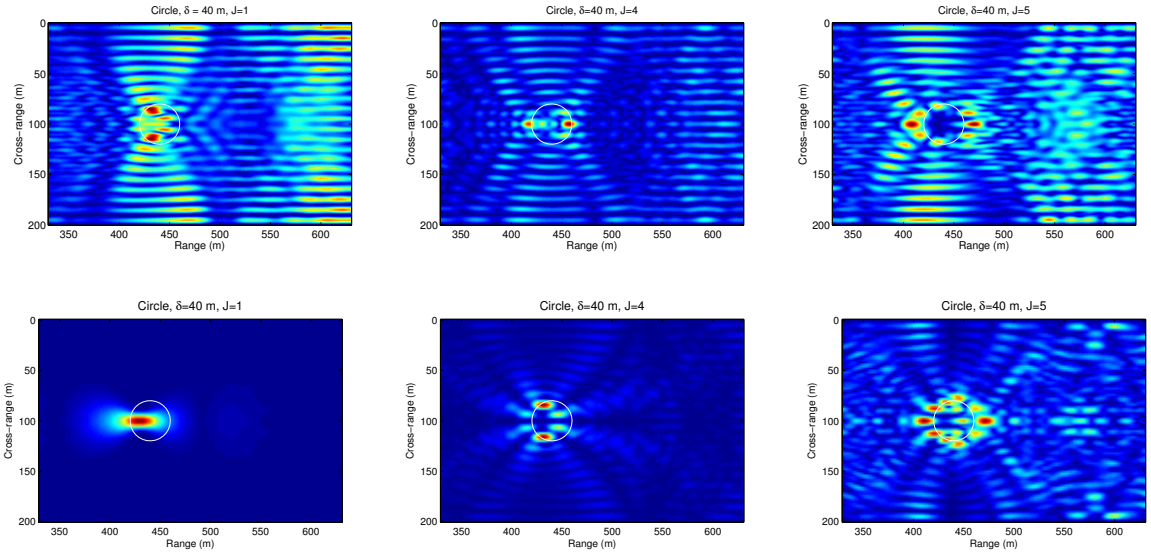

Figure 5: $\mathcal{I}_J^{\mathrm{KM}}$ (top row) versus $\widetilde{\mathcal{I}}_J^{\mathrm{KM}}$ (bottom row) for a circular scatterer with diameter $b = 40$ m. J indicates projection on the Jth singular vector. From left to right $J = 1$, $J = 4$ and $J = 5$.

As a first comment, note that selective imaging with $\widetilde{\mathcal{I}}^{\mathrm{KM}}$ exhibits the expected behaviour (see e.g. [7]), in the sense that the largest singular value is associated to an image focused at the center of the object, while intermediate singular values carry information about the edges.

Test case 2: Circular scatterer with diameter $\delta = 20$ m for a single frequency.
Here we decrease the diameter of the previous circular scatterer to $\delta = \lambda_0 = 20$ m. In Figure 6 we plot the values of $|\mathcal{I}_1^{\mathrm{KM}}(\omega)|$ and $|\widetilde{\mathcal{I}}_1^{\mathrm{KM}}(\omega)|$ (selective imaging with respect to the first singular vector) for single frequencies of 73 Hz (left column) and 74 Hz (right column). For both frequencies $|\widetilde{\mathcal{I}}_1^{\mathrm{KM}}(\omega)|$ focuses towards the front center of the circle, as opposed to $|\mathcal{I}_1^{\mathrm{KM}}(\omega)|$ which focuses towards its edges for $f = 73$ Hz but in the center for $f = 74$ Hz. This kind of lack of robustness has initially motivated us to work with $\widetilde{\mathcal{I}}^{\mathrm{KM}}$ rather than with $\mathcal{I}^{\mathrm{KM}}$.

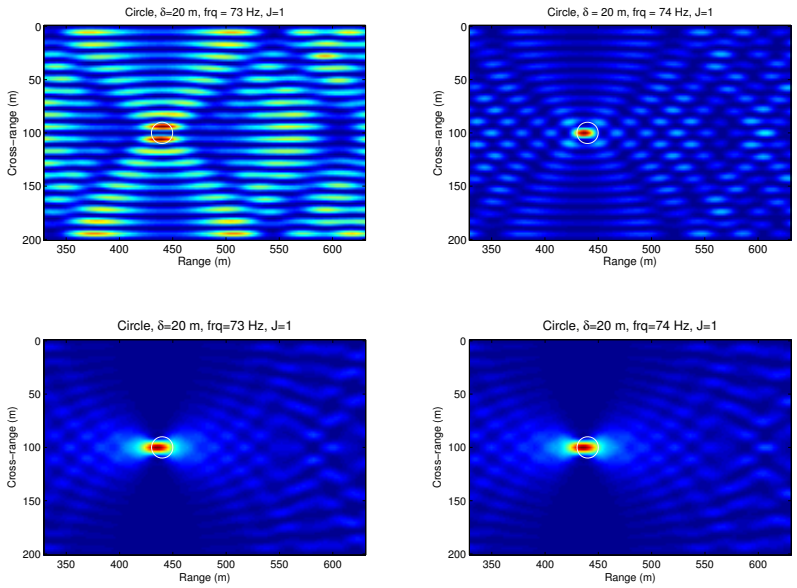

Figure 6: $|\mathcal{I}_1^{\mathrm{KM}}(\omega)|$ (top row) versus $|\widetilde{\mathcal{I}}_1^{\mathrm{KM}}(\omega)|$ (bottom row) for a circle shaped scatterer with diameter $\delta = 20$ m for a single frequencies of 73 Hz (left column) and 74 Hz (right column).

Test case 3: Rhombus shaped scatterer with diameter $\delta = 40$ m
Here we want to assess the performance of $\widetilde{\mathcal{I}}_J^{\mathrm{KM}}$ in a more complex test case. Specifically, we consider a rhombus with diameter $\delta = 40$ m centered at at (440,100) m. In the left subplot of Figure 7 we plot the singular values (normalized with respect to the largest one) of the matrix $\widehat{\mathbb{P}}$ for a frequency equal to 75.5 Hz. Now, the first four singular values are quite close to each other, larger than 80% of the $\sigma_1(\widehat{\mathbb{P}}(\omega))$. The next two are between 30% to 40% of the largest, the seventh is about 10%, and the rest lie below 10%. In the right subplot we plot the values of $\widetilde{\mathcal{I}}^{\mathrm{KM}}$ using the full matrix $\widehat{\mathbb{P}}$. Note that this image carries information also for the support of the scatterer. Figure 8 depicts the values of $\widetilde{\mathcal{I}}_J^{\mathrm{KM}}(\vec{\boldsymbol{y}}^{\mathrm{s}})$ for $J = 1, \ldots, 6$. Clearly, projection on the first singular vector leads to focusing in the center of the object. For $J = 2, 3$ and 4, $\widetilde{\mathcal{I}}_J^{\mathrm{KM}}$ carries information from the bulk and from the edges, while for $J = 5$ and 6, it focuses towards the endpoints of the vertical diameter.

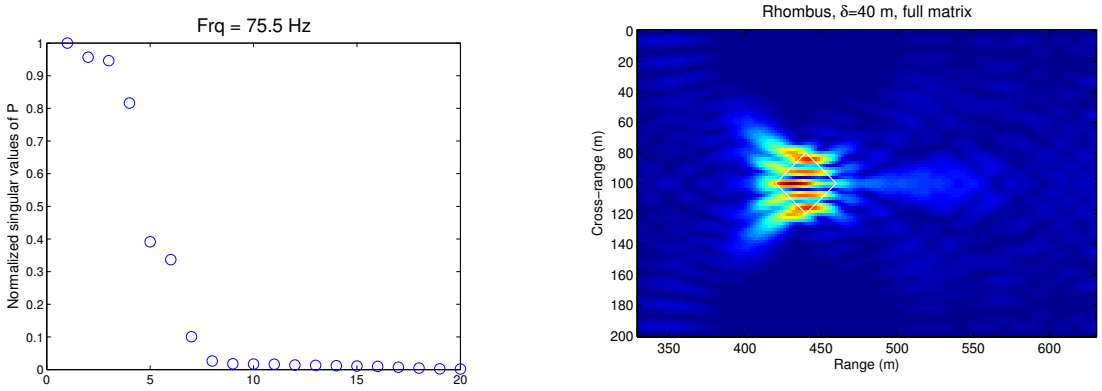

Figure 7: Normalized singular values of $\widehat{\mathbb{P}}$ (left subplot) and $\widetilde{\mathcal{I}}^{\mathrm{KM}}$ for a rhombus shaped scatterer with diameter $b = 40$ m.

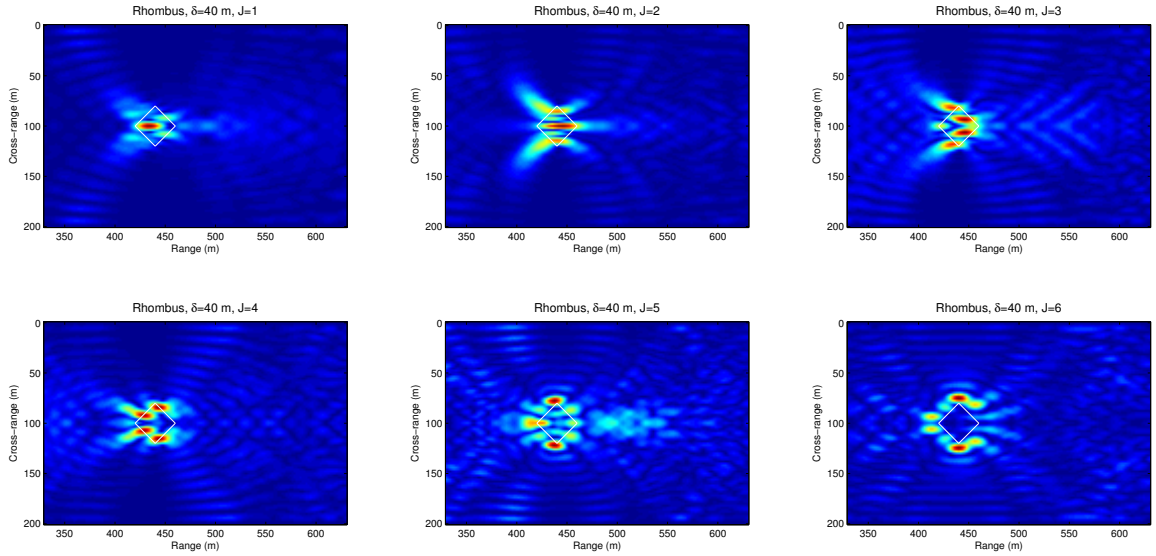

Figure 8: $\widetilde{\mathcal{I}}_J^{\mathrm{KM}}$ for a rhombus shaped scatterer with diameter $\delta = 40$ m. $J = 1, \ldots, 6$, and indicates projection on the Jth singular vector.

Test case 4: Square scatterer with side length $b = 40$ m.
Now, we consider a square scatterer of side length $b = 2\lambda_0 = 40$ m, with its center located at (470,100) m. In this test case we examine the behaviour of $\widetilde{\mathcal{I}}^{\mathrm{KM}}$ and its filtered version under the influence of instrument noise. In order to simulate measurement noise we proceed as in [7] and add a noise matrix $W(\omega)$ with zero mean uncorrelated Gaussian distributed entries with variance $\epsilon p_{\mathrm{avg}}$, *i.e.* $W_{r,s}(\omega) \sim \mathcal{N}(0, \epsilon p_{\mathrm{avg}})$. Here the average power received per source, receiver and frequency is given by

$$p_{\mathrm{avg}} = \frac{1}{N^2 N_{\mathrm{freq}}} \sum_{i=1}^{N_{\mathrm{freq}}} \|\widehat{\Pi}(\omega_i)\|_{\mathrm{F}}^2,$$

where $\|\cdot\|_{\mathrm{F}}$ is the Frobenius matrix norm and N_{freq} the number of frequencies. The expected power of the noise $W(\omega_i)$ over all frequencies, receivers and sources is

$$\mathbb{E}\left[\sum_{i=1}^{N_{\mathrm{freq}}} \|W(\omega_i)\|_{\mathrm{F}}^2\right] = \epsilon N^2 N_{\mathrm{freq}}\, p_{\mathrm{avg}}.$$

Since the total power of the signal received over all frequencies, receivers and sources is $N^2 N_{\mathrm{freq}}\, p_{\mathrm{avg}}$, the Signal-to-Noise Ratio (SNR) in dB is $-10\log_{10}\epsilon$.

As before, we use frequencies ranging from 70.5 to 79.5 Hz with an increment of 1 Hz. In Figure 9 we plot the singular values of the matrices $\widehat{\Pi}$ and $\widehat{\mathbb{P}}$ for the frequency of 75.5 Hz (normalized with respect to the largest one) in the absence of noise and for SNR = 10, 0 and -10 dB. Notice that the singular values that are larger than 20% of the largest one in the case of 10 dB SNR remain close to those corresponding to the unperturbed matrices, while noise has a more profound influence in the singular values of 0 dB and -10 dB SNR.

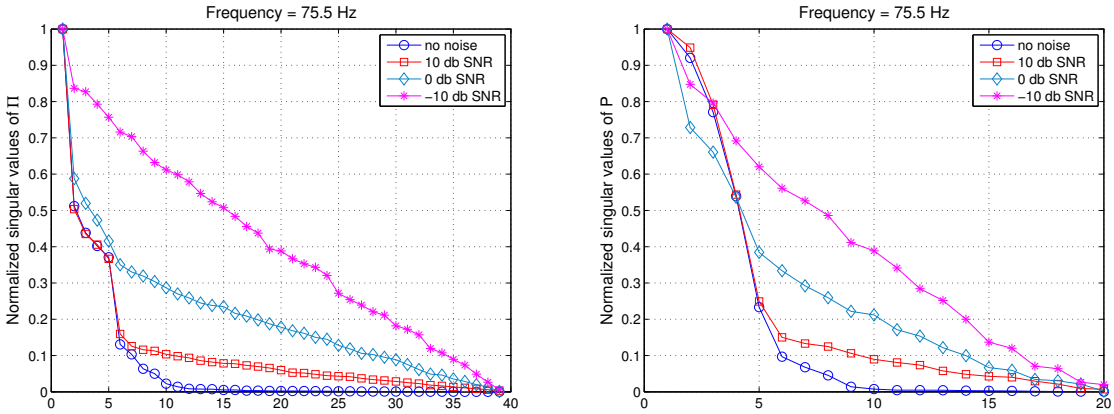

Figure 9: Normalized singular values of $\widehat{\Pi}$ (left subplot) and $\widehat{\mathbb{P}}$ (right subplot) for a square scatterer with side length $b = 40$ m, in the abscence of noise and by adding noise with 10, 0 and -10 dB SNR.

In Figure 10 we plot the images obtained with $\widetilde{\mathcal{I}}^{\mathrm{KM}}$ without using any selective imaging techniques. In all cases the left side of the scatterer is recreated.

Next, we use filtered versions of the matrix $\widehat{\mathbb{P}}$ that employ more than one singular values. These are chosen as follows, [7]:

a) we normalize the singular values with respect to the largest one,

b) we determine an interval $[a, b] \subset (0, 1)$, and

c) we include in the filtered version of $\widetilde{\mathcal{I}}^{\mathrm{KM,f}}$ all the singular values that lie in $[a, b]$.

Figures 11–12 depict the values of $\widetilde{\mathcal{I}}^{\mathrm{KM,f}}$ without noise included and when noise is included with 0 and -10 dB SNR. We do not show the images with 10 dB SNR because they are essentially the same as the ones without noise. Specifically, in Figure 11 we have employed in the computation of $\widetilde{\mathcal{I}}^{\mathrm{KM,f}}$ the singular values that are between 5% and

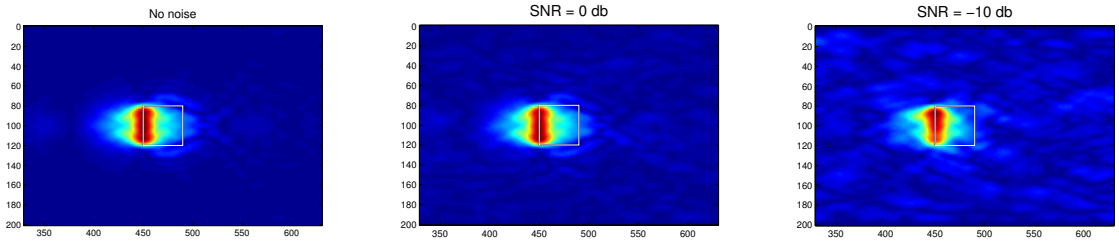

Figure 10: $\widetilde{\mathcal{I}}^{\mathrm{KM}}$ for $b = 40$ m, $D = 200$ m, $c_0 = 1500$ m/s, $f \in [70.5, 79.5]$ Hz and SNR$= \infty, 0, -10$ dB.

60% of the largest one ($[a, b] = [0.05, 0.60]$) and in Figure 12 we take $[a, b] = [0.12, 0.74]$. In both cases the results with 0 dB SNR are qualitatively very similar to those obtained in the absence of noise. Note that even with -10 dB SNR, we are still able to recreate the left side of the object, but the effect of the noise is visible in the image.

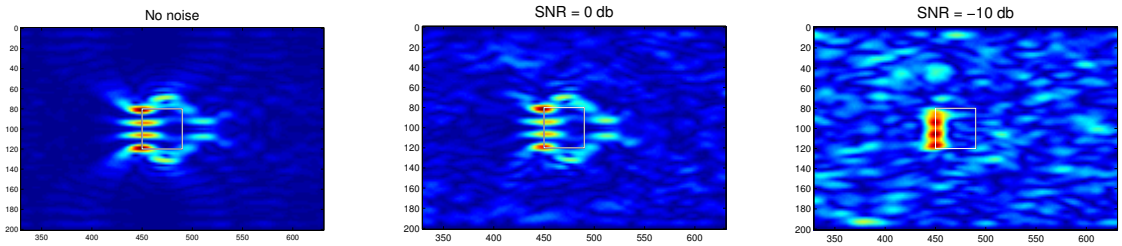

Figure 11: Normalized values of $\widetilde{\mathcal{I}}^{\mathrm{KM,f}}$, for $b = 40$ m, $D = 200$ m, $c_0 = 1500$ m/s, $f \in [70.5, 79.5]$ Hz and SNR$= \infty, 0, -10$ dB, $[a, b] = [0.05, 0.6]$.

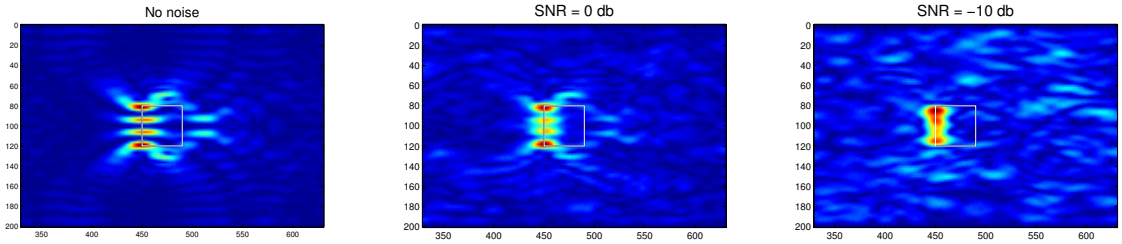

Figure 12: Normalized values of $\widetilde{\mathcal{I}}^{\mathrm{KM,f}}$, for $b = 40$ m, $D = 200$ m, $c_0 = 1500$ m/s, $f \in [70.5, 79.5]$ Hz and SNR$= \infty, 0, -10$ dB, $[a, b] = [0.12, 0.74]$.

5. Analysis of the imaging method

In the present section we consider and analyze a simplified model problem that allows us to obtain some explicit expressions of the array response matrix, thus helping us to investigate and understand the phenomena we have observed in the selective imaging approach of the previous sections.

Specifically, we consider the following model problem: In the marine environment described in Section 2 we assume that the active array passes through the x axis, i.e., the transducers' coordinates are $(0, x_i)$, $x_i = ih$, $1 \le i \le N$, where $h := D/(N+1)$ is the pitch. The target, denoted by $\mathcal{T}$, is assumed to be a vertical one-dimensional perfect reflector, i.e., a 'crack' of width b, located at range $z = L$. The center of the target is denoted by $\vec{\boldsymbol{y}}^* = (L, x_0)$. Let us also denote by $\mathcal{C}$ the vertical section of the waveguide at range $z = L$, i.e., $\mathcal{C} := \{(L, x) : \ 0 \le x \le D\}$. This setup is schematically depicted in Figure 13 and aims at simulating the left side of the square scatterer which we have examined in Section 4. For an analogous setup used to analyze the response matrix for extended targets in the free space we refer to [27].

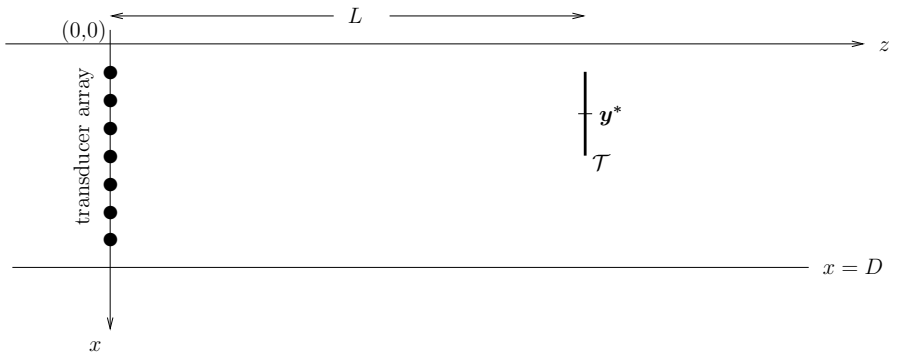

Figure 13: A vertical crack, implemented in the waveguide.

5.1. Array response matrix

Assuming unit reflectivity at each point of the target we may approximate the response in a receiver placed at $\vec{\boldsymbol{x}}_r = (0, x_r)$ due to a source at $\vec{\boldsymbol{x}}_s = (0, x_s)$, $r, s \in \{1, 2, \ldots, N\}$, as

$$\widehat{\Pi}(\vec{\boldsymbol{x}}_r, \vec{\boldsymbol{x}}_s, \omega) = \int_{\mathcal{T}} \widehat{G}(\vec{\boldsymbol{y}}, \vec{\boldsymbol{x}}_r) \widehat{G}(\vec{\boldsymbol{y}}, \vec{\boldsymbol{x}}_s)\, dx, \tag{23}$$

where $\vec{\boldsymbol{y}} = (L, x)$, $x \in [x_0 - b/2, x_0 + b/2]$, and $\widehat{G}$ is the Green's function defined in (5). For future reference, let us also recall that μ_n, X_n are the eigenvalues and corresponding eigenfunctions of the operator $-d^2/dx^2$ in $H^2(0, D) \cap H_0^1(0, D)$, defined in (3), and β_n are the horizontal wavenumbers defined in (4).

Inserting (5) into (23) shows that

$$\widehat{\Pi}(\vec{\boldsymbol{x}}_r; \vec{\boldsymbol{x}}_s, \omega) = -\frac{1}{4} \sum_{m,n=1}^{\infty} \frac{\mathrm{e}^{\mathrm{i}\beta_m L}}{\beta_m} X_m(x_s) X_n(x_r) \frac{\mathrm{e}^{\mathrm{i}\beta_n L}}{\beta_n} \int_{x_0 - \frac{b}{2}}^{x_0 + \frac{b}{2}} X_m(x) X_n(x) dx. \tag{24}$$

Moreover, let $g_m(x_i) := \frac{i}{2}\frac{e^{i\beta_m L}}{\beta_m}X_m(x_i) = \left(\widehat{G}(\cdot,\vec{\boldsymbol{x}}_i), X_m\right)_{L^2(\mathcal{C})}$, where the outer parentheses in the second equality denote the standard L^2 inner product on $\mathcal{C}$. Let us also define $\mathcal{G}$ to be the matrix

$$\mathcal{G} := \begin{pmatrix} g_1(x_1) & g_2(x_1) & \dots & g_M(x_1) & g_{M+1}(x_1) & \dots \\ g_1(x_2) & g_2(x_2) & \dots & g_M(x_2) & g_{M+1}(x_2) & \dots \\ \vdots & \vdots & & \vdots & \vdots & \\ g_1(x_N) & g_2(x_N) & \dots & g_M(x_N) & g_{M+1}(x_N) & \dots \end{pmatrix}$$

and A_{inf} the (infinite) matrix with entries

$$a_{mn} = \int_{x_0-\frac{b}{2}}^{x_0+\frac{b}{2}} X_m(x)X_n(x)dx, \quad m,n = 1,2,\dots\ . \tag{25}$$

Then, using (24), we may write the array response matrix $\widehat{\Pi}$ as a matrix product of the form

$$\widehat{\Pi} = \mathcal{G}A_{\text{inf}}\mathcal{G}^T. \tag{26}$$

We point out that if L is sufficiently large and $m \geq M+1$, then

$$g_m(x_i) = \frac{\mathrm{i}}{2}\frac{\mathrm{e}^{\mathrm{i}\beta_m L}}{\beta_m}X_m(x_i) = \frac{1}{2}\frac{\mathrm{e}^{-\sqrt{\mu_n - k^2}L}}{\sqrt{\mu_n - k^2}}X_m(x_i) \simeq 0,$$

or, in other words, only the principal $N \times M$ part of $\mathcal{G}$ is practically non-zero; thus, in practice, instead of A_{inf} we work with its $M \times M$ principal part denoted by A_M. Note also, that since $h = D/(N+1)$ is the distance between any two consecutive transducers, then for N sufficiently large, the orthonormality of the eigenfunctions infers

$$\begin{aligned}(\mathcal{G}^T\mathcal{G})_{mn} &= -\frac{1}{4}\frac{\mathrm{e}^{\mathrm{i}(\beta_m+\beta_n)L}}{\beta_m\beta_n}\sum_{k=1}^{N} X_m(x_k)X_n(x_k) \\ &\approx -\frac{\mathrm{e}^{\mathrm{i}(\beta_m+\beta_n)L}}{4\beta_m\beta_n}\frac{1}{h}\int_0^D X_m(x)X_n(x)\ dx = -\frac{1}{h}\frac{\mathrm{e}^{\mathrm{i}(\beta_m+\beta_n)L}}{4\beta_m\beta_n}\delta_{mn}.\end{aligned} \tag{27}$$

Hence, $\mathcal{G}^T\mathcal{G}$ is "almost" diagonal, i.e., $\mathcal{G}^T\mathcal{G} \approx \mathcal{D}$, where

$$\mathcal{D}_{mn} = \begin{cases} -\frac{1}{h}\frac{\mathrm{e}^{\mathrm{i}(\beta_m+\beta_n)L}}{4\beta_m\beta_n}, & m = n \\ 0, & m \neq n. \end{cases} \tag{28}$$

Therefore (26) and (27) imply

$$A_{\text{inf}} = \mathcal{D}^{-1}\mathcal{G}^T\widehat{\Pi}\mathcal{G}\mathcal{D}^{-1}. \tag{29}$$

At this point let us remark that although $\widehat{\Pi}$ is associated with A_{inf} (and, in practice, with A_M) through (26), or (29), we cannot infer from these formulae an explicit relation between their singular values.

Next, it is natural to ask how A_M is related to the matrix $\widehat{\mathbb{P}}$ that results when we project the array response matrix $\widehat{\Pi}$ on the propagating modes. Recalling the definition

of $\widehat{\mathbb{P}}$ (14), and using the orthonormality of the eigenfunctions $\{X_n\}_{n=1,2,\ldots}$, one may immediately see that

$$\widehat{\mathbb{P}}_{mn} = -\frac{1}{4}\mathrm{e}^{\mathrm{i}(\beta_m+\beta_n)L}a_{mn}, \quad m,n=1,\ldots,M, \tag{30}$$

or, in matrix form,

$$\widehat{\mathbb{P}} = -\frac{1}{4}QA_MQ, \tag{31}$$

where Q is the diagonal matrix $\mathrm{diag}(\mathrm{e}^{\mathrm{i}\beta_1 L},\ldots,\mathrm{e}^{\mathrm{i}\beta_M L})$. Hence $\widehat{\mathbb{P}}$ is unitarily equivalent to A_M, since $Q^*Q = I$.

5.2. Spectral properties of A_M

Now, we turn our attention to the spectral properties of the real, symmetric matrix A_M, since we have shown that it is related to both matrices $\widehat{\Pi}$ and $\widehat{\mathbb{P}}$ that are involved in the computation of $\mathcal{I}^{\mathrm{KM}}$ and $\widetilde{\mathcal{I}}^{\mathrm{KM}}$, respectively. In what follows we will refer to either the eigenvalues–eigenvectors of A_M or to its singular values–vectors, since the latter are just the former written in descending order.

For $m,n \geq 1$, and in view of the simple trigonometric identity $2\sin a \sin b = \cos(a-b) - \cos(a+b)$, it holds that

$$\begin{aligned} a_{mn} &= \int_{x_0-\frac{b}{2}}^{x_0+\frac{b}{2}} X_m(x)X_n(x)dx = \frac{2}{D}\int_{x_0-\frac{b}{2}}^{x_0+\frac{b}{2}} \sin\frac{m\pi x}{D}\sin\frac{n\pi x}{D}dx \\ &= \frac{1}{D}\int_{x_0-\frac{b}{2}}^{x_0+\frac{b}{2}} \cos\frac{(m-n)\pi x}{D}dx - \frac{1}{D}\int_{x_0-\frac{b}{2}}^{x_0+\frac{b}{2}} \cos\frac{(m+n)\pi x}{D}dx. \end{aligned}$$

Hence

$$A_M = T_M - H_M, \quad \text{where} \quad T_M := (t_{\ell-m})_{\ell,m=1}^M, \quad H_M := (t_{\ell+m})_{\ell,m=1}^M,$$

and

$$t_m = \frac{1}{D}\int_0^D \mathbb{1}_{\mathcal{T}}(x)\cos\frac{m\pi x}{D}dx, \tag{32}$$

where $\mathbb{1}_{\mathcal{T}}(x)$ is the indicator function of $\mathcal{T}$. Note that here $\mathbb{1}_{\mathcal{T}}(x)$ is the so called *generating function* of the matrices A_M, T_M and H_M. One may immediately recognize T_M as a (real symmetric) Toeplitz matrix, i.e., a matrix with constant entries along the diagonals, and H_M as a Hankel matrix, i.e., a matrix with constant skew-diagonals (these are the diagonals that are perpendicular to the main diagonal). Hence A_M is a *Toeplitz–minus–Hankel* matrix. As we shall briefly discuss next, the spectral properties of A_M are determined by the Toeplitz part T_M. This can be seen, for example, by modifying appropriately the proofs in the work of Fasino [10], where he studies the spectral properties of Toeplitz-plus-Hankel matrices, or by tracing back to the work of Trench [25], where he studies the spectral properties of the *real symmetric Toepliz* (RST) matrix

$$T_n = (t_{r-s})_{r,s=1}^n, \quad \text{where } t_r = \frac{1}{\pi}\int_0^\pi f(x)\cos rx\,dx,$$

and the generating function $f \in L^2[0,\pi]$. Following Trench's notation, a vector $\boldsymbol{x} \in \mathbb{R}^n$ is called symmetric if $J\boldsymbol{x} = \boldsymbol{x}$ and skew-symmetric if $J\boldsymbol{x} = -\boldsymbol{x}$, where J is the flip matrix (i.e. the matrix that has ones on the secondary diagonal and zeros elsewhere), see also [2]. Moreover, an eigenvalue λ of T is defined to be even (odd) if T has a symmetric (skew-symmetric) λ–eigenvector.

Now, let $\lambda_1^{(M)} \leq \lambda_2^{(M)} \leq \ldots \leq \lambda_M^{(M)}$ be the eigenvalues of T_M and $\nu_1^{(M)} \leq \nu_2^{(M)} \leq \ldots \leq \nu_M^{(M)}$ be the eigenvalues of A_M. Since, in our case, the generating function f of the matrices A_M, T_M and H_M, is the indicator function of $\mathcal{T}$, its essential lower and upper bounds are simply 0 and 1, respectively, and a result of Szegő, [14, pp. 64, 65], guarantees that i) $0 \leq \lambda_i^{(M)} \leq 1$, for all $i = 1, \ldots, M$, ii) for any fixed integer k, $\lambda_k^{(M)} \to 0$, $\lambda_{M-k}^{(M)} \to 1$, as $M \to \infty$, and iii) if G is any continuous function defined in [0,1] we have

$$\lim_{M\to\infty} \frac{1}{M} \sum_{i=1}^{M} G(\lambda_i^{(M)}) = \frac{1}{D} \int_0^D G(f(x))dx. \tag{33}$$

Moreover, the following theorem specializes results stated in [25] to our case, where we work on $[0, D]$, the entries of our matrix are given in (32), and $f = \mathbb{1}_{\mathcal{T}}$.

Theorem 5.1 *(a) The odd eigenvalues $\kappa_1^{(2M+1)} \leq \kappa_2^{(2M+1)} \leq \ldots \leq \kappa_M^{(2M+1)}$ of T_{2M+1} are the eigenvalues of A_M, [25, Th. 2].*

(b) Since f is bounded the sets $\{\lambda_i^{(M)}\}_{i=1}^M$ and $\{\kappa_i^{(2M+1)}\}_{i=1}^M$ are absolutely equally distributed, [25, Def. 1, Th. 5].

(c) Since f is bounded (33) holds also for $\nu_i^{(M)}$ instead of $\lambda_i^{(M)}$. Moreover, the cardinality of the set $\{i : \epsilon \leq \kappa_i^{(2M+1)} \leq 1 - \epsilon, \text{ for } \epsilon > 0\}$ equals 0.

Summarizing, the eigenvalues of the matrix A_M are clustered emphatically near 0 and 1, and considering the function G to be the identity on $[0, 1]$ we immediately see that

$$\lim_{M\to\infty} \frac{1}{M} \sum_{i=1}^{M} \nu_i^{(M)} = \frac{1}{D} \int_0^D \mathbb{1}_{\mathcal{T}}(x)\, dx = \frac{b}{D}.$$

This indicates that asymptotically as $M \to \infty$ the ratio of the non-zero eigenvalues of A_M to the total number of eigenvalues is equal to b/D. In our case, where M is the number of propagating modes and is equal to $\left\lfloor \frac{2D}{\lambda} \right\rfloor$, it is expected that the number of 'significant' singular values for our matrix is

$$\left[M \frac{b}{D} \right] \approx \left[\frac{2b}{\lambda} \right]. \tag{34}$$

To conclude we have shown, that the number of non-zero singular values is related to the size of the object. Moreover, considering that the resolution in cross-range is $\lambda/2$ (see Figure A1 in the Appendix), then the rank of the matrix (i.e., the number of non-zero singular values) is roughly the size of the object divided by the 'array resolution'. This has been proven for the case of free space (see [7, §4.5.2]), but, to the best of our knowledge, it is a new result concerning a waveguide geometry.

In the next subsection we explore the form of the eigenvectors of A_M, in order to gain some insight about the behaviour of the functionals that we are using for selective imaging.

5.3. Selective imaging

We consider the imaging functional $\widetilde{\mathcal{I}}_J^{\mathrm{KM}}$, where the subscript J indicates that the matrix $\widehat{\mathbb{P}}$ is approximated by means of the J-th singular vector for selective imaging. Then, for a search point $\vec{\boldsymbol{y}}^{\mathrm{s}} = (L, x^{\mathrm{s}})$ located at the correct range L, (21) and (30) imply that

$$\widetilde{\mathcal{I}}_J^{\mathrm{KM}}(\vec{\boldsymbol{y}}^{\mathrm{s}}) = \frac{1}{16h^2} \sum_{m,n=1}^{M} X_m(x^{\mathrm{s}}) X_n(x^{\mathrm{s}}) \sigma_J u_J^m u_J^n = \sigma_J \left(\frac{1}{4h} \sum_{n=1}^{M} u_J^n X_n(x^{\mathrm{s}}) \right)^2, \tag{35}$$

where $\boldsymbol{u}_J = (u_J^1, u_J^2, \ldots, u_J^M)^T$ is the singular vector of A_M that corresponds to the singular value σ_J. Recalling the definition of X_n in (3), and suppressing constants, we associate to $\boldsymbol{u}_J$ the trigonometric polynomial

$$s_J(x) = \sum_{n=1}^{M} u_J^n \sin \frac{n\pi x}{D}.$$

Therefore, the behaviour of $\widetilde{\mathcal{I}}_J^{\mathrm{KM}}$ is in fact determined by the properties of $s_J(x)$, that we shall illustrate in the following example: Consider a waveguide with depth equal to $D = 200$ m and constant sound speed equal to $c_0 = 1500$ m/s. In Figure 14 (left subplot) we plot the singular values of A_M for a frequency of 74 Hz, for which the number of propagating modes $M = 19$, the wavelength $\lambda \approx 20.27$ m, and $\mathcal{T}$ is centered at $x_0 = 70$ m while its width is taken equal to $b = 40$ m $\approx 2\lambda$. According to (34) the number of 'significant' singular values equals 4. Indeed, one may see that the first three remain very close to 1, the fourth one is approximately 0.65 and the fifth lies in the transition layer between 0 and 1 close to 0.3. The sixth one is less than 0.1 while the rest are very close to zero. In the right subplot of Figure 14 we plot the square

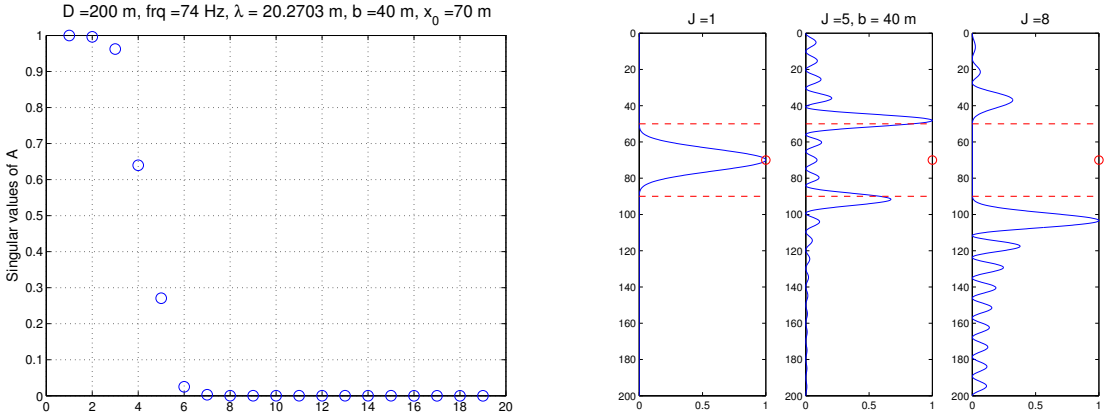

Figure 14: Left: The singular values of A_M ($M = 19$). Right: The graphs of $(s_J(x))^2$, $x \in [0, 200]$, for $J = 1, 5, 8$, normalized with respect to their largest values.

of the values of the trigonometric polynomials $s_J(x)$ for $J = 1, 5$ and 8, normalized with respect to their largest values. The relevant singular vectors $\boldsymbol{u}_J$, $J = 1, 5, 8$ have been computed with MATLAB. The red circle in these figures indicates the center x_0 of $\mathcal{T}$ and the red dashed lines the width b. Note that $s_1(x)$ that corresponds to the first singular value is supported in $\mathcal{T}$ and exhibits a peak at the center x_0, $s_5(x)$ exhibits peaks near the endpoints of $\mathcal{T}$, while $s_8(x)$ is approximately zero for $x \in \mathcal{T}$. These remind us the spectral properties and the band-limited behaviour of the so called *prolate matrix*, see [24, 26, 15]. As remarked in [15] for the prolate matrix, one may characterize the eigenspace corresponding to eigenvalue cluster near 1 as the *signal subspace*, the eigenspace corresponding to eigenvalue cluster near 0 as the *noise subspace* and the eigenspace corresponding to eigenvalues in the intermediate layer as the *transient subspace*; the terminology is adopted by [15].

Next, we try to explore the form of the singular vectors (eigenvectors) of A_M. To this end, we consider an orthonormal basis $\{Y_j(x)\}_{j=1}^{\infty}$ of $L^2[x_0 - b/2, x_0 + b/2]$; specifically, let $Y_j(x) = \sqrt{\frac{2}{b}} \sin\left(\frac{(x-x_0+\frac{b}{2})j\pi}{b}\right)$, $j = 1, 2, \ldots$. Then, the restriction of the eigenfunctions $X_n \in L^2[0, D]$ on the crack $\mathcal{T}$ may be written as

$$X_n(x)|_{[x_0-b/2,x_0+b/2]} = \sum_{j=1}^{\infty} v_j^n Y_j(x), \text{ where } v_j^n = \int_{x_0-\frac{b}{2}}^{x_0+\frac{b}{2}} X_n(x) Y_j(x)\, dx.$$

The orthonormality of the Y_i's and Parseval's relation imply that

$$a_{mn} = (X_m, X_n)_{L^2(\mathcal{T})} = \sum_i (X_m, Y_i)_{L^2(\mathcal{T})} (X_n, Y_i)_{L^2(\mathcal{T})} = \sum_{i=1}^{\infty} v_i^m v_i^n. \tag{36}$$

Let us define

$$\boldsymbol{v}_i = (v_i^1, v_i^2, \ldots, v_i^M, \ldots)^T, \tag{37}$$

and note that the sequences $\boldsymbol{v}_i \in l_2$, for every i. Then the infinite matrix A_{inf} may be written as

$$A_{\text{inf}} = \sum_{i=1}^{\infty} \boldsymbol{v}_i \, \boldsymbol{v}_i^T. \tag{38}$$

Moreover, the $\boldsymbol{v}_i$ are orthonormal. Indeed, let $\langle \cdot, \cdot \rangle$ denote the standard inner product in l_2, and $\widetilde{Y}_i$ the extension by zero of Y_i on $[0, D]$. Then

$$\begin{aligned} \langle \boldsymbol{v}_i, \boldsymbol{v}_j \rangle = & \sum_{n=1}^{\infty} v_i^n v_j^n = \sum_n (X_n, Y_i)_{L^2(\mathcal{T})} (X_n, Y_j)_{L^2(\mathcal{T})} \\ = & \sum_n (\widetilde{Y}_i, X_n)_{L^2[0,D]} (\widetilde{Y}_j, X_n)_{L^2[0,D]} \\ \overset{\text{Parseval}}{=} & (\widetilde{Y}_i, \widetilde{Y}_j)_{L^2[0,D]} = (Y_i, Y_j)_{L^2(\mathcal{T})} = \delta_{ij}. \end{aligned}$$

Now, let V be the closure of $\text{span}\{\boldsymbol{v}_i\}_{i=1,2,\ldots}$. Then $l_2 = V \oplus V^{\perp}$, and A_{inf} is a projection operator where its only eigenvalues are 0 and 1.

Next thing is to investigate the relation between the eigenvectors $\boldsymbol{u}_j$ of A_M that correspond to eigenvalues close to 1, and the eigenvectors $\boldsymbol{v}_j$ of A_{inf} corresponding to the

eigenvalue 1. Let us multiply, for example, A_M by the vector consisting of the M first components of $\boldsymbol{v}_j$, (i.e., $\left(v_j^1, v_j^2, \ldots, v_j^M\right)^T$). The i-th component of the resulting vector is equal to

$$\begin{aligned}\sum_{k=1}^{M} a_{ik} v_j^k &= \sum_{k=1}^{\infty} a_{ik} v_j^k - \sum_{k=M+1}^{\infty} a_{ik} v_j^k \\ &= \sum_{k=1}^{\infty} (X_i, X_k)_{L^2(\mathcal{T})} (X_k, Y_j)_{L^2(\mathcal{T})} - \sum_{k=M+1}^{\infty} a_{ik} v_j^k \\ &= \sum_{k=1}^{\infty} (X_i \mathbb{1}_{\mathcal{T}}, X_k)_{L^2[0,D]} (\widetilde{Y}_j, X_k)_{L^2[0,D]} - \sum_{k=M+1}^{\infty} a_{ik} v_j^k \\ &= \sum_{k=1}^{\infty} (X_i \mathbb{1}_{\mathcal{T}}, \widetilde{Y}_j)_{L^2[0,D]} - \sum_{k=M+1}^{\infty} a_{ik} v_j^k = v_j^i - \left(\sum_{k=M+1}^{\infty} a_{ik} v_j^k \right).\end{aligned}$$

The last term above in the parenthesis is $O(1/M)$, hence if the j-th singular value is approximately 1, then $\left(v_j^1, v_j^2, \ldots, v_j^M\right)^T$ approximates $\boldsymbol{u}_j$, i.e., the j-th singular vector of A_M. This is illustrated in Figure 15 where we plot the components of the first two singular vectors $\boldsymbol{u}_J$, $J = 1, 2$, of A_M and the M first terms of the sequences $\boldsymbol{v}_J$, $J = 1, 2$, for the parameters of the previous example for which $M = 19$.

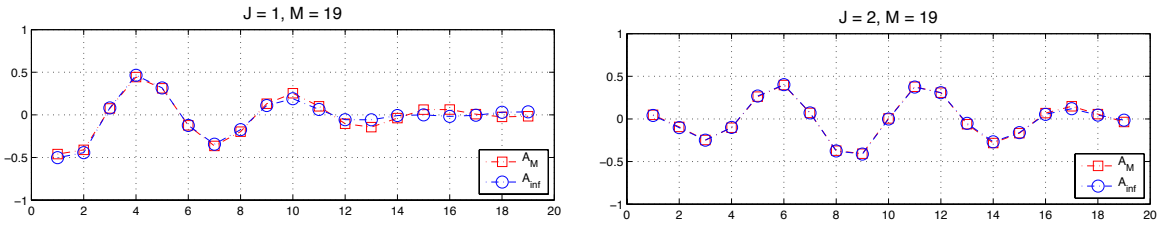

Figure 15: The singular vector $\boldsymbol{u}_J$ of A_M (its components are marked with red squares) vs. the M first terms of $\boldsymbol{v}_J$ marked with blue circles, for $J = 1$ (left) and $J = 2$ (right).

Hence, as long as J is associated to a singular vector that lies in the signal subspace, one may approximate $\widetilde{\mathcal{I}}_J^{\mathrm{KM}}$ as

$$\widetilde{\mathcal{I}}_J^{\mathrm{KM}}(\vec{\boldsymbol{y}}^{\mathrm{s}}) \approx \sum_{m,n=1}^{M} X_m(x^{\mathrm{s}}) X_n(x^{\mathrm{s}}) v_J^m v_J^n = \left(\sum_{n=1}^{M} v_J^n X_n(x^{\mathrm{s}}) \right)^2, \tag{39}$$

where constants are once more suppressed. Moreover, letting $M \to \infty$, we get that

$$\begin{aligned}(\widetilde{\mathcal{I}}_J^{\mathrm{KM}}(\vec{\boldsymbol{y}}^{\mathrm{s}}))^{1/2} &\approx \left| \sum_{n=1}^{\infty} v_J^n X_n(x^{\mathrm{s}}) \right| = \left| \sum_{n} (X_n, Y_J)_{L^2(\mathcal{T})} X_n(x^{\mathrm{s}}) \right| \\ &= \left| \sum_{n} (\widetilde{Y}_J, X_n)_{L^2[0,D]} X_n(x^{\mathrm{s}}) \right| = |\widetilde{Y}_J(x^{\mathrm{s}})|. \end{aligned} \tag{40}$$

Using the specific form of the Y_J we get that as long as the J-th s.v. is close to one, then

$$\widetilde{\mathcal{I}}_J^{\mathrm{KM}}(\vec{\boldsymbol{y}}^{\,\mathrm{s}}) \approx \frac{2}{b}\sin^2\left(\frac{(x^{\mathrm{s}}-x_0+\frac{b}{2})J\pi}{b}\right). \tag{41}$$

In the remaining of this section, we will compare these asymptotic results with the outcome of some numerical simulations.

5.4. Numerical experiments

Next, we present some results for the simplified model of the vertical one dimensional scatterer (the crack). Specifically, a) we compare results of selective imaging with $\widetilde{\mathcal{I}}_J^{\mathrm{KM}}$ with those obtained using the asymptotic formulae (39), (41), and b) we compare results between selective imaging with $\mathcal{I}_J^{\mathrm{KM}}$ and $\widetilde{\mathcal{I}}_J^{\mathrm{KM}}$. In all the following examples the sound speed is taken equal to $c_0 = 1500$ m/s and the depth of the waveguide equal to $D = 200$ m.

5.4.1. $\widetilde{\mathcal{I}}_J^{\mathrm{KM}}$ versus asymptotics

First, we consider a single frequency $f = 74$ Hz, hence the wavelength $\lambda \approx 20.27$ m. The array has $N = 39$ receivers, the pitch $h = 5$ m $\simeq \lambda/4$ and the crack, centered at $(L, x_0) = (410, 70)$ m, has length $b = 40$ m $\simeq 2\lambda$. The number of propagating modes in the waveguide is $M = 19$. The singular values of A_M are shown in Figure 14. We have seen previously that A_M and, consequently, the matrix $\widehat{\mathbb{P}}$ defined in (30), have $[2b/\lambda] = 4$ significant singular values. In other words, and with reference to Figure 14, it is expected that the first three singular vectors comprise the signal subspace, the fourth and the fifth lie in the transient subspace, and the rest correspond to the noise subspace.

We now turn to check the validity of the asymptotic expressions (39) and (41). In Figure 16 we plot superimposed the normalized graphs of $\widetilde{\mathcal{I}}_J^{\mathrm{KM}}(\vec{\boldsymbol{x}}^{\,\mathrm{s}}, \omega)$ (see (21)), of (39) and of (41), for $\vec{\boldsymbol{x}}^{\,\mathrm{s}}$ that are located at the correct range L, and for $J = 1$ and 2. The subscript J indicates that only the J-th singular vector is employed in the filtered version of the matrix $\widehat{\mathbb{P}}$, defined in (30). As one may immediately see there is good agreement between the numerics and the asymptotic expressions.

In Figure 17 we show analogous results for selective imaging with $\widetilde{\mathcal{I}}_J^{\mathrm{KM}}(\vec{\boldsymbol{x}}^{\,\mathrm{s}}, \omega)$ and (39), based on the third to the sixth singular vectors. Now, one may notice somewhat larger discrepancies but, in general, the asymptotic expression agrees well with the numerical results for $J = 3$, 4 and 5. For $J = 6$ there is a clear mismatch, with $\widetilde{\mathcal{I}}_J^{\mathrm{KM}}$ focusing approximately 4.5 m below the lower endpoint of the crack, since now the corresponding singular vector belongs to the noise subspace. (The discrepancies, as expected, are even larger between the results of $\widetilde{\mathcal{I}}_J^{\mathrm{KM}}(\vec{\boldsymbol{x}}^{\,\mathrm{s}}, \omega)$ and (41), and we do not include them in the figure. These discrepancies may be attributed to the fact that the asymptotic analysis is based on matrices of order n, where $n \to \infty$, while in the numerics only their principal $M \times M$ part has been taken into account. For example,

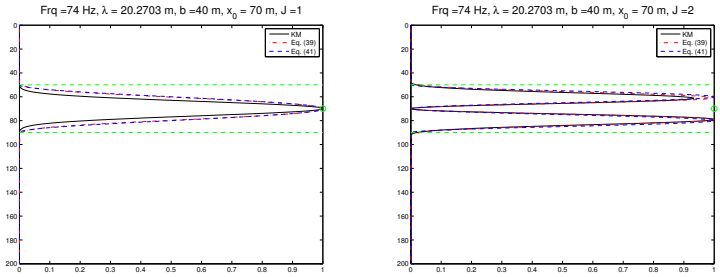

Figure 16: The graph of $\widetilde{\mathcal{I}}_J^{\mathrm{KM}}((L,x^{\mathrm{s}}),\omega)$ (solid black line) normalized and superimposed on the graphs of (39) (dash-dotted red line) and (41) (dashed blue line). J indicates projection on the Jth singular vector. The ordinate $x_0-b/2$ and $x_0+b/2$ are in dashed green lines, and x_0 is marked with a green circle. Here $c_0=1500$ m/s, $f=74$ Hz, $D=200$ m, $b=40$ m, $x_0=70$ m and $J=1$ (left subplot), $J=2$ (right subplot).

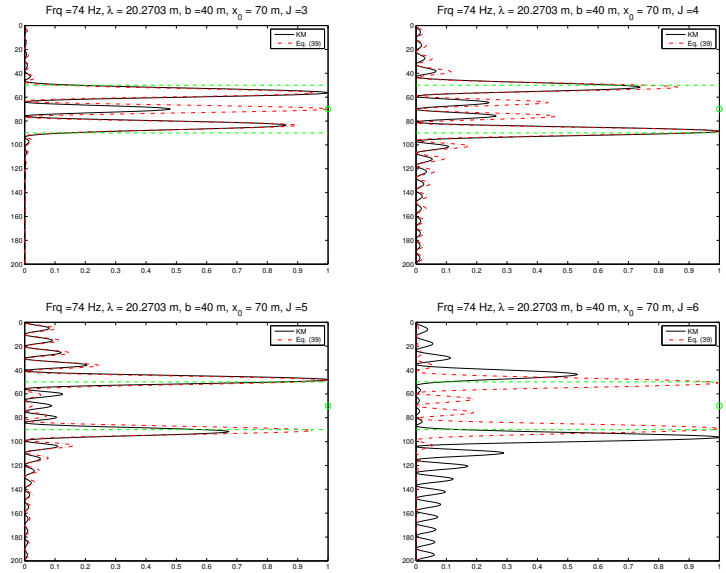

Figure 17: The graph of $\widetilde{\mathcal{I}}_J^{\mathrm{KM}}((L,x^{\mathrm{s}}),\omega)$ (solid black line) superimposed on the graph of (39) (dash-dotted red line). J indicates projection on the Jth singular vector and the ordinate $x_0-b/2$ and $x_0+b/2$ are in dashed green lines, while x_0 is marked with a green circle. Here $J=3,4,5$ and 6, $c_0=1500$ m/s, $f=74$ Hz, $D=200$ m, $b=40$ m, $x_0=70$ m.

the orthogonality of $\boldsymbol{v}_i$ (see (37)) is valid only for the infinite matrix A_{inf} and is expected to hold only approximately for fixed n.)

Figures 16 and 17, suggest that selective imaging with $\widetilde{\mathcal{I}}_J^{\mathrm{KM}}(\omega)$ by means of the first singular vector focuses in the middle of the object, while the fourth and the fifth singular vectors are focusing mainly in the lower and the upper endpoint of the crack, respectively.

5.4.2. $\mathcal{I}_J^{\mathrm{KM}}$ versus $\widetilde{\mathcal{I}}_J^{\mathrm{KM}}$

Next, we compare selective imaging with $\mathcal{I}_J^{\mathrm{KM}}$ versus $\widetilde{\mathcal{I}}_J^{\mathrm{KM}}$, keeping the same setup as in Section 5.4.1.

In the top row of Figure 18 we plot the modulus of $\mathcal{I}_J^{\mathrm{KM}}(\omega)$ (see (11)), for $J = 1, 2, 4$ and 5, and in the bottom row the corresponding results for the modulus of $\widetilde{\mathcal{I}}_J^{\mathrm{KM}}(\omega)$ (see (21)). As before J indicates projection on the Jth singular vector, and the search domain is $[350, 470] \times [10, 130]$ (all distances are in meters). Note the robustness in the results of $\widetilde{\mathcal{I}}_J^{\mathrm{KM}}(\omega)$, where projection on the first singular vector focuses in the center of the crack as projection on subsequent singular vectors results in focusing towards the edges, as opposed to those of $\mathcal{I}_J^{\mathrm{KM}}(\omega)$.

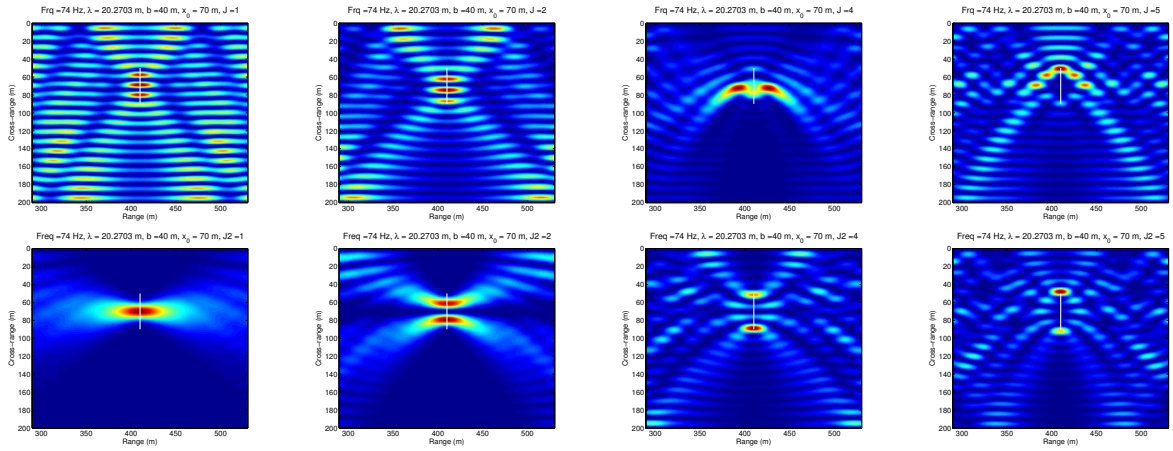

Figure 18: Values of $\mathcal{I}_J^{\mathrm{KM}}(\omega)$ (top row) and $\widetilde{\mathcal{I}}_J^{\mathrm{KM}}(\omega)$ (bottom row) for the crack, where $J = 1, 2, 4, 5$ and it indicates projection on the Jth singular vector.

The theoretical analysis and the numerical results shown in this section for the model problem of an one dimensional reflector are in agreement and help us understand the selective imaging results presented in Section 4 in the more general case of extended two dimensional reflectors.

6. Concluding remarks

In this paper we considered the problem of selective imaging extended reflectors in a waveguide using an active array of sensors. To this end, we proposed a novel selective imaging functional based on Kirchhoff migration and the singular value decomposition of $\widehat{\mathbb{P}}(\omega)$, which is a weighted modal projection of the array response matrix. The proposed imaging method has been theoretically analyzed for a simplified model of a vertical one-dimensional reflector of width b, and the following main results were derived:

(i) We showed that the rank of $\widehat{\mathbb{P}}(\omega)$ is approximately equal to $[\frac{b}{\lambda/2}]$, that is, the size of the reflector divided by the array resolution $\lambda/2$ (λ being the wavelength at frequency ω). This result has been recently proven in free space (cf. [7, §4.5.2]), but, to the best of our knowledge, it is a new result for waveguides.

(ii) We derived analytic expressions for the singular vectors of $\widehat{\mathbb{P}}(\omega)$, as well as for our selective imaging functional. Exploiting these expressions we showed that imaging using the projection of $\widehat{\mathbb{P}}(\omega)$ on its first singular vector exhibits focusing in the center of the reflector, while by projecting on the last significant singular vector we create an image that focuses in the endpoints of the reflector. Again our results are in agreement with those obtained in free space (cf. [7]).

Moreover, the results obtained for this simplified model show good agreement when compared with those derived in the more involved case of a square scatterer.

One of the main assumptions that is essential for the construction of the proposed imaging functional and for the subsequent analysis is that the array spans the whole waveguide, a hypothesis that is probably not realistic in applications. Therefore it would be very interesting to generalize this approach to the case of partial array aperture. This does not seem at all straightforward. For example, for a partial array aperture, key properties like the orthonormality of the vertical eigenfunctions X_n along the array fail to hold.

Appendix A. Resolution analysis for a point scatterer

Resolution analysis is a classical way to assess the performance of an imaging method and relies on studying the behaviour of the *point spread function (PSF)*, i.e., of the imaging functional for a *point* scatterer. We consider here an array passing through the x axis and a point scatterer placed far enough from the array at $\vec{\boldsymbol{x}}^* = (z^*, x^*)$. Then, for a source located at $\vec{\boldsymbol{x}}_s = (0, x_s)$ and a receiver at $\vec{\boldsymbol{x}}_r = (0, x_r)$ we may approximate the (r, s) entry of the response matrix for the scattered field by

$$\widehat{\Pi}(\vec{\boldsymbol{x}}_r, \vec{\boldsymbol{x}}_s, \omega) = \tau(\omega)\widehat{G}(\vec{\boldsymbol{x}}^*, \vec{\boldsymbol{x}}_s, \omega)\widehat{G}(\vec{\boldsymbol{x}}_r, \vec{\boldsymbol{x}}^*, \omega). \tag{A.1}$$

In (A.1), we ignore the direct waves going from $\vec{\boldsymbol{x}}_s$ to $\vec{\boldsymbol{x}}_r$ and assume that the scattered field is simply the Green's function from $\vec{\boldsymbol{x}}_s$ to $\vec{\boldsymbol{x}}^*$ multiplied by the scattering coefficient $\tau(\omega)$ and then by the Green's function from $\vec{\boldsymbol{x}}^*$ to $\vec{\boldsymbol{x}}_r$. In what follows, we assume for simplicity that our scatterer is an isotropic point reflector with $\tau(\omega) = 1$. Next, we replace the expression for the Green's function given by (5) into (A.1) taking into account only the propagating modes, and get

$$\widehat{\Pi}(\vec{\boldsymbol{x}}_r, \vec{\boldsymbol{x}}_s, \omega) = -\frac{1}{4}\sum_{k=1}^{M}\sum_{\ell=1}^{M}\frac{\mathrm{e}^{\mathrm{i}\beta_k z^*}}{\beta_k}X_k(x_s)\frac{\mathrm{e}^{\mathrm{i}\beta_\ell z^*}}{\beta_\ell}X_\ell(x_r)X_k(x^*)X_\ell(x^*). \tag{A.2}$$

For a $\vec{\boldsymbol{y}}^{\mathrm{s}} = (z^{\mathrm{s}}, x^{\mathrm{s}})$ in our search domain, the imaging functional (6) becomes

$$\mathcal{I}^{\mathrm{KM}}(\vec{\boldsymbol{y}}^{\mathrm{s}}, \omega) = \frac{1}{16}\sum_{s,r=1}^{N}\sum_{m,n=1}^{M}\sum_{m',n'=1}^{M}\frac{\mathrm{e}^{\mathrm{i}(\beta_m+\beta_n)z^*}}{\beta_m\beta_n}X_m(x_s)X_n(x_r)X_m(x^*)X_n(x^*)\times$$
$$\times\frac{\mathrm{e}^{-\mathrm{i}(\beta_{m'}+\beta_{n'})z^{\mathrm{s}}}}{\beta_m\beta_n}X_{m'}(x_s)X_{n'}(x_r)X_{m'}(x^{\mathrm{s}})X_{n'}(x^{\mathrm{s}}). \tag{A.3}$$

Assuming that the array spans the whole depth of the waveguide with an array pitch h small enough, we can approximate the double sum with respect to s and r in (A.3),

by a double integral over x_s and x_r, and use the orthonormality of the eigenfunctions X_n to obtain

$$\mathcal{I}^{\rm KM}(\vec{\boldsymbol{y}}^{\rm s},\omega) \approx \left(\frac{1}{4h} \sum_{n=1}^{M} \frac{\mathrm{e}^{\mathrm{i}\beta_n(z^*-z^{\rm s})}}{\beta_n^2} X_n(x^*) X_n(x^{\rm s}) \right)^2 . \tag{A.4}$$

On the other hand, using (A.2) the matrix $\widehat{\mathbb{P}}$, defined in (17), takes the form

$$\widehat{\mathbb{P}}_{mn}(\omega) = -\frac{1}{4} \mathrm{e}^{\mathrm{i}\beta_m z^*} \mathrm{e}^{\mathrm{i}\beta_n z^*} X_m(x^*) X_n(x^*).$$

Hence, in view of the above relation, (16) reduces to

$$\widetilde{\mathcal{I}}^{\rm KM}(\vec{\boldsymbol{y}}^{\rm s},\omega) = \left(\frac{1}{4h} \sum_{n=1}^{M} \mathrm{e}^{\mathrm{i}\beta_n(z^*-z^s)} X_n(x^*) X_n(x^{\rm s}) \right)^2 . \tag{A.5}$$

Appendix A.1. Cross-range resolution for $\widetilde{\mathcal{I}}^{\rm KM}(\omega)$

To examine the resolution in cross-range, we assume that the wavelength λ is much smaller than the depth ($\lambda \ll D$) and that the search point is located at the correct range, i.e., $z^{\rm s} = z^*$. Then, recalling (3), the imaging functional (A.4) simplifies to

$$\mathcal{I}^{\rm KM}(\vec{\boldsymbol{y}}^{\rm s};\omega) = \left(\frac{1}{2Dh} \sum_{n=1}^{M} \frac{1}{\beta_n^2} \sin\frac{n\pi x^*}{D} \sin\frac{n\pi x^{\rm s}}{D} \right)^2 , \tag{A.6}$$

while (A.5) takes the form

$$\widetilde{\mathcal{I}}^{\rm KM}(\vec{\boldsymbol{y}}^{\rm s};\omega) = \left(\frac{1}{2Dh} \sum_{n=1}^{M} \sin\frac{n\pi x^*}{D} \sin\frac{n\pi x^{\rm s}}{D} \right)^2 . \tag{A.7}$$

We have the following result:

Lemma 1 *(A.7) can be approximated by*

$$\widetilde{\mathcal{I}}^{\rm KM}(\vec{\boldsymbol{y}}^{\rm s};\omega) \approx \left[\frac{1}{2\lambda h} \left(\mathrm{sinc}\Big(\tfrac{2}{\lambda}(x^*-x^{\rm s})\Big) - \mathrm{sinc}\Big(\tfrac{2}{\lambda}(x^*+x^{\rm s})\Big) \right) \right]^2 , \tag{A.8}$$

where $\mathrm{sinc}(x) = (\sin(\pi x))/(\pi x)$.

Proof: Letting $\xi_n = \lambda n/(2D)$ we approximate the sum over n in (A.7) by an integral. Therefore, from (A.7) we have

$$\begin{aligned}
\widetilde{\mathcal{I}}^{\rm KM}(\vec{\boldsymbol{y}}^{\rm s};\omega) &\approx \left[\frac{1}{\lambda h} \int_0^1 \sin\left(\frac{2\pi x^* \xi_n}{\lambda}\right) \sin\left(\frac{2\pi x^s \xi_n}{\lambda}\right) d\xi_n \right]^2 \\
&= \left\{ \frac{1}{2\lambda h} \int_0^1 \left[\cos\left(\frac{2\pi(x^*-x^s)}{\lambda} x\right) - \cos\left(\frac{2\pi(x^*+x^s)}{\lambda} x\right) \right] dx \right\}^2 \\
&= \left[\frac{1}{2\lambda h} \left(\mathrm{sinc}\Big(\tfrac{2}{\lambda}(x^*-x^{\rm s})\Big) - \mathrm{sinc}\Big(\tfrac{2}{\lambda}(x^*+x^{\rm s})\Big) \right) \right]^2 .
\end{aligned} \tag{A.9}$$

■

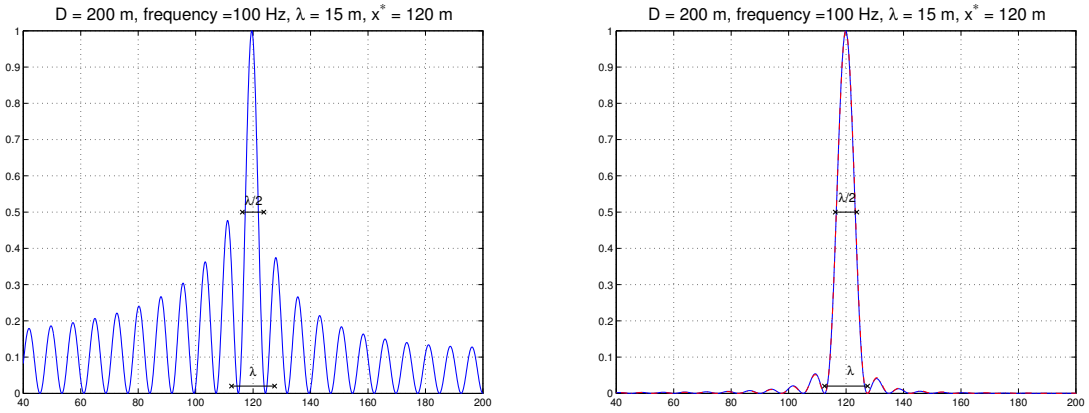

Figure A1: Left subplot: The graph of (A.6) for $D = 200$ m, $f = 100$ Hz, $c_0 = 1500$ m/s, $x^* = 120$ m. Right subplot: The graph of (A.7) (solid blue line) superimposed on the graph of (A.8) (dashed red line), for the same parameters.

In the left subplot of Figure A1 we plot the normalized modulus of the imaging functional (A.6) for $D = 200$ m, $c_0 = 1500$ m/s, $x^* = 120$ m and frequency 100 Hz, in the cross-range window [40,200] (in meters). In the right subplot we superimpose for the same parameters the graphs of (A.7) and (A.8), normalized with respect to their maximum values. As one may see $\widetilde{\mathcal{I}}^{\rm KM}$ exhibits considerably lower side lobes than $\mathcal{I}^{\rm KM}$, albeit $\mathcal{I}^{\rm KM}$'s main lobe is slightly narrower than that in $\widetilde{\mathcal{I}}^{\rm KM}$.

Appendix A.2. Range resolution for $\widetilde{\mathcal{I}}^{\rm KM}(\omega)$

In order to estimate the resolution in range we assume that the search point is located at the correct depth, i.e. at $\vec{\boldsymbol{y}}^{\rm s} = (z^{\rm s}, x^*)$, and, for simplicity, that the scatterer is placed at half the depth of the waveguide, i.e., $x^{\rm s} = x^* = D/2$.

Then, the imaging functional (A.4) takes the form

$$\mathcal{I}^{\rm KM}(\vec{\boldsymbol{y}}^{\rm s},\omega) = \left(\frac{1}{2Dh} \sum_{n=0}^{\lceil \frac{M}{2} \rceil - 1} \frac{\mathrm{e}^{\mathrm{i}\,\beta_{2n+1}(z^*-z^s)}}{\beta_{2n+1}^2} \right)^2 , \tag{A.10}$$

and similarly, (A.5) becomes

$$\widetilde{\mathcal{I}}^{\rm KM}(\vec{\boldsymbol{y}}^{\rm s},\omega) = \left(\frac{1}{2Dh} \sum_{n=0}^{\lceil \frac{M}{2} \rceil - 1} \mathrm{e}^{\mathrm{i}\,\beta_{2n+1}(z^*-z^s)} \right)^2 . \tag{A.11}$$

Lemma 2 *(A.11) can be approximated by*

$$\widetilde{\mathcal{I}}^{\rm KM}(\vec{\boldsymbol{y}}^{\rm s},\omega) \approx \left\{ \frac{1}{2\lambda h} \left[1 - \tfrac{\pi}{2}\, \mathbf{H}_1\Big(\tfrac{2\pi}{\lambda}(z^*-z^{\rm s})\Big) + \mathrm{i}\, \tfrac{\pi}{2}\, J_1\Big(\tfrac{2\pi}{\lambda}(z^*-z^{\rm s})\Big) \right] \right\}^2 , \tag{A.12}$$

where $J_1(x)$ and $H_1(x)$ denote the Bessel and Struve function of order one, respectively, [1].

Proof: Let $\left(n+\frac{1}{2}\right)\frac{\lambda}{D}=\xi_n$. Then $\beta_{2n+1}=\frac{2\pi}{\lambda}\sqrt{1-\xi_n^2}$ and the sum in the right-hand side of (A.11) may be approximated by

$$\mathcal{I}^{\rm KM}(\vec{\boldsymbol{y}}^{\rm s},\omega)\approx\left(\frac{1}{2\lambda h}\int_0^1 \mathrm{e}^{\mathrm{i}\frac{2\pi}{\lambda}(z^*-z^s)\sqrt{1-x^2}}\,dx\right)^2. \tag{A.13}$$

Letting $\alpha=2\pi(z^*-z^s)/\lambda$, we want to evaluate the integral $\int_0^1 \mathrm{e}^{\mathrm{i}\alpha\sqrt{1-x^2}}\,dx$. To this end, letting $x=\sin\theta$ we have

$$\begin{aligned}\int_0^1 \mathrm{e}^{\mathrm{i}\,\alpha\sqrt{1-x^2}}\,dx &\approx \int_0^{\pi/2}\mathrm{e}^{\mathrm{i}\alpha\cos\theta}\cos\theta\,d\theta\\ &=\int_0^{\pi/2}\cos(\alpha\cos\theta)\cos\theta\,d\theta+\mathrm{i}\int_0^{\pi/2}\sin(\alpha\cos\theta)\cos\theta\,d\theta=:I_1+\mathrm{i}\,I_2\end{aligned}$$

In I_2 we change variables $\theta=\frac{\pi}{2}-x$ to obtain

$$I_2=\int_0^{\pi/2}\sin(\alpha\sin x)\sin x\,dx=\frac{\pi}{2}J_1(\alpha),$$

where the integral is found in [12, (3.715.2)].

For I_1 we integrate by parts

$$I_1=\int_0^{\pi/2}\cos(\alpha\cos\theta)(\sin\theta)'\,d\theta=1-\alpha\int_0^{\pi/2}\sin(\alpha\cos\theta)\sin^2\theta\,d\theta=1-\frac{\pi}{2}\,\mathbf{H}_1(\alpha).$$

For the last integral above see [12, (3.716.16)]. Finally, we have that

$$\widetilde{\mathcal{I}}^{\rm KM}(\vec{\boldsymbol{y}}^{\rm s},\omega)\approx\left[\frac{1}{2\lambda h}\left(1-\frac{\pi}{2}\,\mathbf{H}_1(\alpha)+i\frac{\pi}{2}J_1(\alpha)\right)\right]^2. \tag{A.14}$$

■

In Figure A2 we plot the modulus of the imaging functional (A.10) (left subplot) and the modulus of (A.11) versus the modulus of the graph of (A.12) (right subplot), normalized with respect to their maximum values, for $D=200$ m, $c_0=1500$ m/s, $z^*=480$ m and frequency 100 Hz, in the range window [380,580] (in meters). Note that for $\mathcal{I}^{\rm KM}$ the width of the PSF is about 2λ at less than 10% of its maximum value, while for $\widetilde{\mathcal{I}}^{\rm KM}$ the width becomes 2λ at about 20% of its maximum value.

Remark 1 *The plots in Figures A1 and A2 show the point spread function (PSF) of $\mathcal{I}^{\rm KM}$ and $\widetilde{\mathcal{I}}^{\rm KM}$ as a function of cross-range and range, respectively. We observe that the PSF is centered at the correct location of the scatterer. The resolution of the imaging method can be determined using these plots. If we define, for example, the resolution as the width of the PSF at half its maximal value we obtain a cross-range resolution of $\lambda/2$ (see Figure A1).*

Acknowledgments

We would like to thank Dr Adrien Semin for his invaluable help with Montjoie and Prof. M. Papadimitrakis for fruitful discussions on Toeplitz operators. The work of C. Tsogka was partially supported by the European Research Council under the European Union's

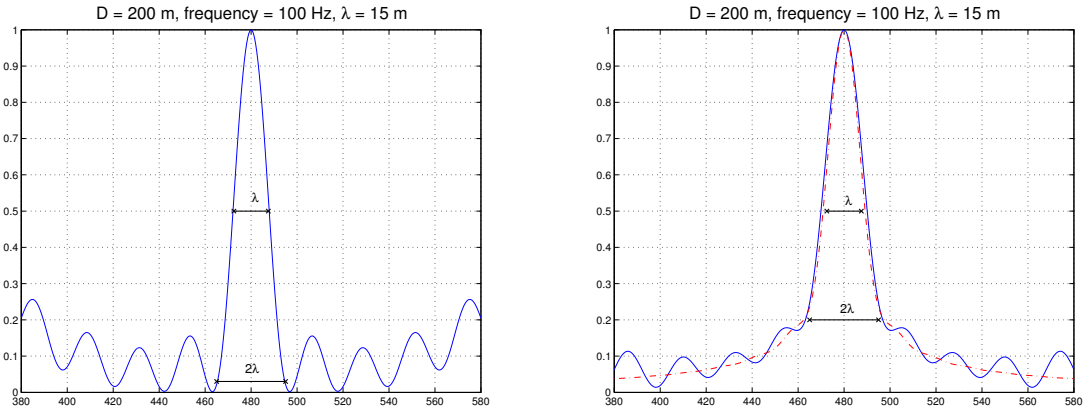

Figure A2: Left subplot: The graph of (A.10) for $D = 200$ m, $f = 100$ Hz, $c_0 = 1500$ m/s, $z^* = 480$ m. Right subplot: The graph of (A.11) (solid blue line) superimposed on the graph of (A.12) (dashed red line), for the same parameters.

Seventh Framework Programme (FP7/2007-2013) / ERC grant agreement n. 239959. D. Mitsoudis was partially supported by the European Union's Seventh Framework Programme (FP7-REGPOT-2009-1) under grant no. 245749 through the Archimedes Center for Modeling, Analysis and Computation (ACMAC) of the Department of Applied Mathematics at the University of Crete.

References

[1] Abramowitz M Stegun IA (eds) 1972, *Handbook of Mathematical Functions with Formulas, Graphs, and Mathematical Tables* (New York: Dover)

[2] Andrew AL 1973 Eigenvectors of certain matrices *Linear Algebra Appl* **7** 151–162

[3] Berenger J-P 1994 A perfectly matched layer for he absorption of electromagnetic waves *J Comput Phys* **114** 185–200

[4] Bleistein N, Cohen JK and Stockwell JW Jr 2001 *Mathematics of Multidimensional Seismic Imaging,Migration, and Inversion* (New York: Springer)

[5] Borcea L, Papanicolaou G and Tsogka C 2007 Optimal waveform design for array imaging *Inverse Problems* **23** 1973-2020

[6] Borcea L, Papanicolaou G and Tsogka C 2007 Optimal illumination and waveform design for imaging in random media *J Acoust Soc Am* **122** 3507–3519

[7] Borcea L, Papanicolaou G and Guevara Vasquez F 2008 Edge illumination and imaging of extended reflectors *SIAM J Imaging Sci* **1** 75-114

[8] Borcea L, Papanicolaou G and Tsogka C 2010 Subspace projection filters for imaging in random media *Comptes Rendus Mécanique* **338** 390–401

[9] Gedney SD 1996 An anisotropic perfectly matched layer-absorbing medium for the truncation of FDTD lattices *IEEE Trans Antennas Propag* **44** 1630–1639.

[10] Fasino D 1996 Spectral properties of Toeplitz-plus-Hankel matrices *Calcolo* **33** 87–98

[11] Golub GH and Van Loan CF 1996 *Matrix Computations* (Baltimore: Johns Hopkins University Press)

[12] Gradshteyn IS and Ryzhik IM 2007 *Table of Integrals, Series, and Products* 7th edition (New York: Academic Press)

[13] Gray RM 2001 *Toeplitz and Circulant Matrices: A Review* Technical report, Information Systems Laboratory, Stanford University

[14] Grenander U and Szegő G 1984 *Toeplitz Forms and their Applications* (New York: AMS Chelsea Publishing)

[15] Hanke M and Nagy J 1998 Inverse Toeplitz preconditioners for ill-posed problems *Linear Algebra Appl* **284** 137–156

[16] Hazard C and Ramdani K 2004 Selective acoustic focusing using time-harmonic reversal mirrors *SIAM J Appl Math* **64** 1057–1076

[17] Jensen FB, Kuperman WA, Porter MB and Schmidt H 2004 *Computational Ocean Acoustics* (New York: Springer)

[18] Kuperman WA and Jackson D 2002 Ocean Acoustics, Matched-Field Processing and Phase Conjugation *Imaging of Complex Media with Acoustic and Seismic Waves* (*Topics in Applied Physics* vol 84) ed M Fink, WA Kuperman, J-P Montagner and A Tourin (Berlin/Heidelberg: Springer) 43–97

[19] Montjoie user's guide `http://montjoie.gforge.inria.fr/`

[20] Mordant N, Prada C, and Fink M 1999 Highly resolved detection in a waveguide with the D.O.R.T. method *J Acoust Soc Am* **105** 2634–2642

[21] Pinçon B and Ramdani K 2007 Selective focusing on small scatterers in acoustic waveguides using time reversal mirrors *Inverse Problems* **23** 1–25

[22] Prada C and Fink M 1994 Eigenmodes of the time reversal operator: A solution to selective focusing in multiple-target media *Wave Motion* **20** 151–163

[23] Prada C, De Rosny J, Clorennec D, Minonzio JG, Aubry A, Fink M, Bernière L, Hibral S, Billand P and Folégot T, 2007 Experimental detection and focusing in shallow water by Decomposition of the Time Reversal Operator *J Acoust Soc Am* **122** 761–768

[24] Slepian D 1978 Prolate spheroidal wave functions, Fourier analysis and uncertainty V: The discrete case, *Bell Syst. Tech. J.* **57** 1371–1430

[25] Trench W 1999 Asymptotic distribution of the even and odd spectra of real symmetric Toeplitz matrices *Linear Algebra Appl* **302-303** 155–162

[26] Varah JM 1993 The prolate matrix *Linear Algebra Appl* **187** 269–278

[27] Zhao H 2004 Analysis of the response matrix for an extended target *SIAM J Appl Math* **64** 725–745